

# Scalable Fabrication of Micro-Architected Water Filtering Membranes

Thesis by  
Andrew C. Friedman

In Partial Fulfillment of the Requirements for  
the degree of  
Doctor of Philosophy

The Caltech logo, featuring the word "Caltech" in a bold, orange, sans-serif font.

CALIFORNIA INSTITUTE OF TECHNOLOGY  
Pasadena, California

2023  
(Defended May 23<sup>rd</sup>, 2023)

© 2023

Andrew C. Friedman

## ACKNOWLEDGEMENTS

In my time at Caltech, I have been fortunate to have had the best colleagues a budding scientist could ask for. My research group has been an incredible source of excitement and inspiration, and I cannot express how thankful I am to have found my way to the lifelong friends I have made. I am particularly thankful for the exemplary advice, guidance and support provided to me by my advisor, Prof. Julia Greer. Her unique blend of rigor and compassion provided the ideal environment for me to grow creatively and become a proper scientist while she provided steadfast support both personally and professionally.

Additionally, I would like to acknowledge the support of my esteemed thesis committee: Profs. Zhen-Gang Wang, Mikhail Shapiro, and Konstantinos Giapis; I thank you for your expertise, insights, and criticisms. I would like to additionally thank other members of the Caltech community that have had meaningful and positive impact on my journey: Allison Kinard, Christy Jenstad, Dr. Giada Spigolon, and Dr. Guy DeRose for their sage advice and help along the way. Lastly, I would like to thank my irreplaceable and incredible polymer chem mentor, Dr. Jeong Hoon Ko; thank you for your consistent availability and help throughout my PhD journey.

Thank you immensely to the Greer group, both past and present, for providing a fun and engaging environment to both work and play. From late nights in the lab to late nights playing board games, I thank you. Thank you to Dr. Daryl Yee for putting up with my never-ending list of questions and guiding me as I took my first steps into polymers and microfabrication. Thank you to Dr. Luizetta Elliott for being my go-to ideas springboard, and for providing a fun break from work over a game of Terraforming Mars. Thank you to Dr. Max Saccone for being an excellent officemate and for providing exactly the right advice whenever I needed it. Thank you to Dr. Rebecca Gallivan for her friendship, her kindness, and for being my SEM troubleshooting hotline. Thank you to Dr. Matias Kagias for his friendship, intellectual and emotional support, and for helping me fully realize the goals of the

scalability project. Thank you to Akash, Nikhil, Seneca, Cyrus, and the rest of the polymers subgroup for your insights and for providing a safe environment to discuss the toughest problems I encountered in grad school.

Finally, I want to thank my family for their unwavering support as I trekked through what has been inarguably the most difficult journey I have ever undertaken. Thank you to my dad, who inspired me to constantly push boundaries and become a scientist; thank you to my mom for her love and support; thank you to my sister for reminding me not to take life too seriously and being my best friend through thick and thin. Thank you to Elina for her warmth and love; I'm not sure I would have made it to this point without her presence in my life. And thank you of course to my dearest Lulu, who has been a constant source of happiness during even my darkest times, and for whom I work every day in hopes that I make her world a better place. Last, but certainly not least, thank you to my wonderful girlfriend Sara, to whom I am forever indebted for her unending love and emotional support. Thank you for being a constant source of smiles and for giving me a reason to get out of bed on my worst days.

## ABSTRACT

Polymer-based filtration devices are predominantly mass manufactured via mechanical spinning or electrospinning of heated polymer materials or fiberglass to create a randomly oriented fibrous network. This technique, while effective at producing materials necessary for traditional filtering applications, fails to afford control over morphology, both macro- and microscopically. The filtering material produced often relies exclusively on its randomly assembled porosity (and occasionally on its surface charge) to capture materials from filtered fluids but provides little means for targeted analyte capture without bulk surface coating or functionalization. This thesis seeks to demonstrate a unique approach to filtration membrane manufacture via a novel high-throughput holographic lithography and contact lithography process in the visible spectrum that utilizes a customized negative-tone photoresist inherently capable of localized surface modification.

This thesis first describes the development of a large-scale holographic lithography process, from conceptualization to implementation, and demonstrates its efficacy by examining produced materials. A phase metasurface mask is utilized to produce a periodic intensity distribution of incident photons. This mask is irradiated at 0.23-0.25 W via linear raster scanning of a 2.2 mm diameter 532 nm laser at 1.5 mm/s and a scan offset of 0.4 mm to produce a homogeneous exposure profile in visible-light sensitized SU-8 negative-tone photoresist. Subsequent photoresist development results in 30–40  $\mu\text{m}$ -thick nano-architected sheets with  $2.1 \times 2.4 \text{ cm}^2$  lateral dimensions and  $\sim 500 \text{ nm}$ -wide struts organized in layered 3D brick-and-mortar-like patterns to result in  $\sim 50\text{--}70\%$  porosity. Scanning electron micrographs of cross-sectioned materials reveal how pattern morphology varies with cure depth, and furthermore how the lack of complete porosity disqualifies this material for application as a membrane filter.

This thesis subsequently focuses on the development of a novel glycidyl methacrylate (GMA)-based negative-tone photoresist for implementation in the previously

described lithography system to produce materials more amenable to functional membrane filter production. GMA is polymerized with a photo-caged aminated monomer, 2-((((2-nitrobenzyl)oxy)carbonyl)amino)ethyl 2-methyloxirane-2-carboxylate (ONBAMA) via free radical polymerization (FRP) and atom-transfer radical polymerization (ATRP) to produce ~30 kDa statistical co-polymers at an 85:15 monomer ratio, respectively. These linear co-polymers are then mixed with a photoacid generator (PAG) to produce a 532 nm sensitized negative-tone photoresist. Pre- and post-exposure bake temperatures are selected via glass-transition temperature identification (~62 °C) with differential scanning calorimetry (DSC) experiments, and cure depth varying with optical exposure dose is examined via establishment of contrast curves. The photoresist is then utilized in the previously described lithography system to produce square arrays of ~25 μm circular holes, and the resulting films are characterized via optical and scanning electron microscopy.

This thesis concludes with an examination of the poly(GMA-*rand*-ONBAMA) films implemented as water-permeable filtration membranes. Efficacy of surface functionalization and solution capture explored via amine deprotection and subsequent tagging with fluorescein isothiocyanate (FITC) dye. The presence and intensity uniformity of tagged samples are examined via confocal microscopy. Transmission of water is justified analytical examination and phenomenologically demonstrated via droplet loading of supported membranes with methylene blue-dyed water. Results are preliminary but indicate potential application of manufactured films as water filters.

In summary, this thesis provides a foundation for the development of nano- and micro-architected materials at large scale and details its implementation for the design and preliminary testing of a GMA-based photoresist for water filtering membrane manufacture. Future research on optimizing photoresist design for mechanical stability could enable utilization of similar membranes for protein capture from biological fluids for use in diagnostic tools and assay automation.

## PUBLISHED CONTENT AND CONTRIBUTIONS

M. Kagias, S. Lee, A. C. Friedman, et al. “Metasurface-Enabled Holographic Lithography for Impact-Absorbing Nanoarchitected Sheets.” *Advanced Materials*, 2209153 (2023).  
DOI: <https://doi.org/10.1002/adma.202209153>.

A. C. F. co-developed the material fabrication techniques and peripheral methods, aided in designing the experiments, produced samples for experiments, and participated in writing the manuscript.

## TABLE OF CONTENTS

Acknowledgements	iii
Abstract	v
Published Content and Contributions	vii
Table of Contents	viii
List of Illustrations	x
Chapter 1: Introduction	1
1.1 Filtration	1
1.2 Fabrication Techniques	2
1.3 Objectives	4
Chapter 2: High-Throughput Large-Area Holographic Lithography	6
2.1 Holographic Lithography to Produce Nano-Architected Materials	6
2.2 Metasurfaces for Advancing Holographic Lithography	9
2.3 Constituent Material: SU-8	10
2.4 Lithography Method Development	12
2.4.1 Optical Apparatus and Raster Optimization	12
2.4.2 Exposure & Processing Conditions	14
2.5 Fabrication & Microstructural Characterization	15
2.5.1 Results	15
2.5.2 Discussion	17
2.6 Experimental Methods	19
2.7 Summary & Outlook	20
Chapter 3: Custom Epoxide-Based Functionalizable Photoresist	23
3.1 Photoresist Classification & Mechanisms	23
3.2 Custom Photoresist Monomer Selection & Design Goals	26
3.3 Photoresist Processing	27
3.4 Surface Functionalization	31
3.5 Photoresist Formulation & Pre-Polymer Synthesis	34
3.6 Processing Optimization & Performance	38
3.6.1 Photoresist Processing	38
3.6.2 Lithographic Performance	47
3.7 Experimental Methods	49
3.8 Summary & Outlook	53
Chapter 4: Water Filter Design & Characterization	55
4.1 Filter Design	54
4.2 Hydrophilicity & Water Permeability	58
4.3 Deprotection Verification & Surface Characterization	60
4.4 Experimental Methods	63
4.5 Summary & Outlook	65
Chapter 5: Summary & Outlook	68
5.1 Summary	67

	ix
5.2 Future Updates to Photoresist Processing & Formulation	69
5.3 Future Application: Protein Capture	72
Bibliography	74

## LIST OF ILLUSTRATIONS

1.1	Membrane filtration technique summary	1
2.1	Holographic lithography and representative products	8
2.2	Metasurface mask and interference pattern	10
2.3	SU-8 photoresist constituents	10
2.4	Visible light photoacid generation	11
2.5	Metasurface-enable holographic lithography apparatus	12
2.6	Raster scan optimization	14
2.7	Morphology and pattern fidelity	16
2.8	SU-8 film curling	22
3.1	Acid-catalyzed cationic ring-opening polymerization	25
3.2	Glycidyl methacrylate monomer	26
3.3	Epoxide-based photoresist processing steps	28
3.4	ONBAMA synthesis and deprotection	33
3.5	Synthesized ONBAMA <sup>1</sup> H NMR	34
3.6	Free radical polymerization mechanism of styrene	36
3.7	Co-polymer <sup>1</sup> H NMR	36
3.8	Solvent content of soft-baked films with temperature ramp	41
3.9	Micrographs of initial dosing experiments exhibiting heat damage	42
3.10	Optical dose contrast curve	43
3.11	Differential scanning calorimetry of PGRO	45
3.12	Varied PEB durations	46
3.13	25 um pore matrix resolved in PGRO photoresist	47
4.1	Filtration mask and resulting structure	55
4.2	Delaminated filtration membrane	57
4.3	Water contact angle experiments	58
4.4	Droplet diameter vs time	59
4.5	Solid phase PGRO deprotection	61
4.6	Confocal fluorimetry of FITC treated PGRO membranes	62
5.1	Surface biotinylation of PGRO	73

## Chapter 1

### INTRODUCTION

#### 1.1 Filtration

Filtration is, at its simplest, the process by which contaminant matter is removed from a fluid stream via pressure-driven passage through a porous, often tortuous, solid-phase network, and it exists as one of the oldest developed separations techniques still scientifically and industrially practiced. The specific analyte or size-scale a filter is designed to target indicates the regime within a particular filtration technique can be categorized, ranging from small molecule and ion filtration via reverse osmosis (RO) up through bacterial filtration via micro-filtration (MF), capped by simple particle filtration. These techniques have a wide range of applications in water purification,<sup>[1]</sup> food processing,<sup>[2]</sup> biotechnology,<sup>[3]</sup> and pharmaceutical manufacturing.<sup>[4]</sup>

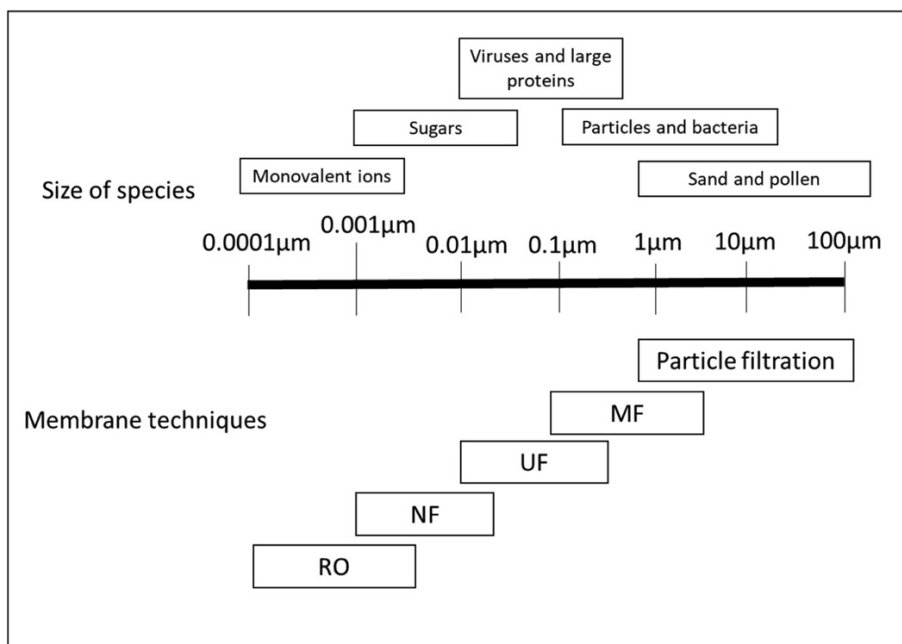


**Figure 1.1:** Membrane filtration technique summary. Different filtration techniques, their relevant size-scale, and typical target are indicated. *Reproduced with permission.*<sup>[5]</sup>

Regardless of the targeted analytes or size scale (outside of osmotic filtration), filtration typically falls into one of two categories, either via particle obstruction/rejection or through affinity-based capture. The former relies on the fact that particles of sufficient size (i.e., larger than the effective pore size) cannot pass through the tortuous path presented by the solid filter's matrix, trapping the contaminant and preventing its flow into the resulting filtrate. The latter relies on chemical affinity toward the analyte by electrostatic interaction,<sup>[6]</sup> host-guest interaction,<sup>[7]</sup> hydrogen bonding,<sup>[8]</sup> among other potential mechanisms. Direct pressure-driven membrane filters can be categorized into two major classes: porous ceramic and polymeric. The ceramic filters exhibit greater mechanical and thermal resilience<sup>[9]</sup> but have up-front energetic costs in manufacturing compared with their polymeric counterparts, which exhibit a wider range of potential functionality and diversity in structural design and implementation.<sup>[10]</sup> Research into filtration membranes over the past decade primarily focuses on wastewater purification, which matches the most abundant industrial application of filtration as well. This comes at a time where focuses on water sustainability and drinking water production from wastewater products have become top priorities in water management policy worldwide.<sup>[5]</sup> The overwhelming majority of recent research into polymer-based microfiltration appears to focus on the manufacture of novel materials and modifications of existing ones to facilitate better filtrate permeability while providing resistance to fouling and analyte capture selectivity. In contrast, little research has been done regarding manufacturing techniques and how filter geometry affects figures of merit.

## ***1.2 Fabrication Techniques***

Polymer filtration membranes, as they exist today, are almost entirely manufactured via stochastic processes that yield randomly porous polymer networks. Such techniques include phase inversion, whereby a polymer is spontaneously precipitated from the vapor phase by introducing the contained solution to an excess of poor

solvent vapor. Thermally mediated techniques exist for polymer solutions in liquid phase as well. The resulting film is a random assortment of porous structures with features sizes attributed in large part to processing conditions such as temperature, pressure, and fluid agitation velocity.<sup>[11]</sup> While the process is scalable in that filters of arbitrary size can be generated, no control is afforded over filter microstructure, and the technique itself relies on several hazardous and environmentally unfriendly solvents. The next most common technique for membrane filter manufacture is electrospinning, in which a viscoelastic thermoplastic polymer solution is ejected continuously in a stream in the presence of a strong electric field. The electric field overcomes surface tension forces and causes fluid instability, resulting in the solution jet stretching and warping thin enough to spontaneously induce localized solvent evaporation. This yields polymer fibers on the micro- to nano- scale randomly oriented and entangled, producing a highly tortuous network. Membranes produced this way are highly porous, however control of pore size is difficult and often a wide range results from the process.<sup>[12]</sup> While other techniques exist to produce filtration membranes, the two discussed herein are overwhelmingly the most common. Films produced this way have clear and realized industrial applications, but little progress has been made in advancing control over pore morphology.<sup>[11]</sup> Those that do explore ordered and architected filtration membranes note high advantageous properties such as control of flow patterns,<sup>[13]</sup> better anti-fouling properties, more robust mechanical properties, and improved hydrophilicity<sup>[12]</sup> over traditionally manufactured filters; however a considerable drawback is universally discussed: scalability. The techniques employed, such as photolithography, ablation, and self-assembly, are described as labor intensive, difficult to perform at scale, and relatively slow to produce filtration materials, and consequently have not been industrially adapted.<sup>[14]</sup> Within this thesis, we plan to address this concern directly and propose a scalable lithography technique for ordered membrane filter manufacture.

The techniques employed in these studies are typically characterized by the assembly of a 3D structure from its constituent parts rather than creation via the macroscopic

reshaping of a bulk material, better known as “additive manufacturing.” Encapsulated within this description are a wide array of techniques, many of which result in the patterning of polymeric materials, including but not limited to: traditional stereolithography (SLA), multi-photon lithography (MPL), electron-beam lithography (EBL), and interference lithography. These techniques rely on localized energetic excitation of chemical species to cross-link monomers/oligomers and create a macroscopically patterned structure from a polymer melt or solution. Inherent to lithographic techniques is the ability to create complex 3D structures unachievable by more conventional means of manufacture, with length scales ranging from hundreds of microns down to tens of nanometers; this fine control of micro/nanostructure affords control over material properties via deliberate and informed small-scale architecture (for example, a micro/nanolattice).<sup>[15]</sup> The primary limitation to utilizing AM-produced nano-architected materials in many applications is that available AM techniques do not provide acceptable throughput for large-scale production and use in potential devices. Standard lithographic methods of AM are inherently dichotomous in that processes with high throughput lack high resolution regarding minimum feature size, while smaller feature sizes tend to require impractically longer processing times. SLA 3D printers can produce multiple cubic centimeters of patterned material per hour but have minimum feature sizes of ~10 microns, while conversely EBL and MPL utilize sub-micron voxels to create nano-scale features, but because assembly occurs voxel-by-voxel, production rates are unreasonable for large-scale applications.

### ***1.3 Objectives***

The advantages of exploring architected polymer filtration membranes are evident: they afford unparalleled and effective control over filter performance while simultaneously are highly amenable to surface functionalization for targeted analyte rejection and capture, however no technique has arisen to facilitate large-scale production of such membranes. The central theme of this will therefore be the

development of large-scale, high-throughput technique for the manufacture of micro-architected, fluid permeable membranes capable of facile surface functionalization for the targeting of specific analytes within a contaminated water sample. I envision that demonstrating the feasibility and efficacy of scalably-produced architected filters will enable the adoption of these superior filtering materials to commercial and industrial applications. The second chapter will discuss the development of a large-scale holographic lithography technique for the manufacture of micro- and nano-architected materials. Following this, the third chapter will discuss the development and characterization of a photoresist material for use in this technique designed specifically to produce hydrophilic materials for filtration. Finally, the fourth chapter will discuss the evaluation of the produced membranes as filters, after which in chapter five we discuss the implications and next set of necessary experiments for further development of this novel technology.

## Chapter 2

# HIGH-THROUGHPUT LARGE-AREA HOLOGRAPHIC LITHOGRAPHY

Adapted in part from:

M. Kagias, S. Lee, A. C. Friedman, et al. “Metasurface-Enabled Holographic Lithography for Impact-Absorbing Nanoarchitected Sheets.” *Advanced Materials*, 2209153 (2023). DOI: <https://doi.org/10.1002/adma.202209153>.

A. C. F. co-developed the material fabrication techniques and peripheral methods, aided in designing the experiments, produced samples for experiments, and participated in writing the manuscript.

### ***2.1 Holographic Lithography to Produce Nano-Architected Materials***

Unlike most lithographic techniques, holographic lithography (HL) does not pattern element-by-element but instead produces an entire structure in a single exposure. This is accomplished via the utilization of phase-shifted light interference to generate a 2- or 3-dimensional periodic intensity distribution of incident photons. The light interference is either achieved by intersecting multiple independent light beams, often originating from a single source beam to maintain phase control, or by the utilization of a diffractive mask that splits a single incoming beam into multiple diffracted orders that interfere coherently. The optical apparatus to accomplish this beam interference is engineered such that the interference region coincides within a photosensitive material (a photoresist), either cross-linking or photochemically deprotecting it, depending on the positive/negative character of the photoresist. After removal of soluble material, a periodic nano-scale pattern consisting of the photoresist material remains. Because material is patterned in bulk rather than additively, HL is uniquely positioned a technique that can produce large areas of material with nano-scale features.

Due to the scale of the technique, HL is perfectly suited for nano-scale materials manufacture. An example of maskless HL is the work of Miyake *et al.* and Park *et al.* who utilized the technique to produce 3-dimensional photonic crystals,<sup>[16-17]</sup> both with feature sizes below 1  $\mu\text{m}$ . An example of phase mask-enabled HL is the work of Bagal *et al.* who utilized 3D colloidal nano-lithography<sup>[18]</sup> to produce 1  $\mu\text{m}$  thick nano-porous metal oxide films, utilizing a single layer of colloidal nanoparticles as a phase shifting photolithographic mask to achieve the necessary beam splitting and interference.<sup>[19]</sup> Another example is the work of Bae *et al.* who utilized a binary phase-modulating photomask to produce 4 x 4  $\text{in}^2$  regions with 600 nm periodic patterns in 10 micrometer thick negative-tone photoresist via a single laser exposure.<sup>[20]</sup> Representative samples are shown in Figure 1.1b-e. Note in all examples the lack of interconnected pores necessary for filtration applications.

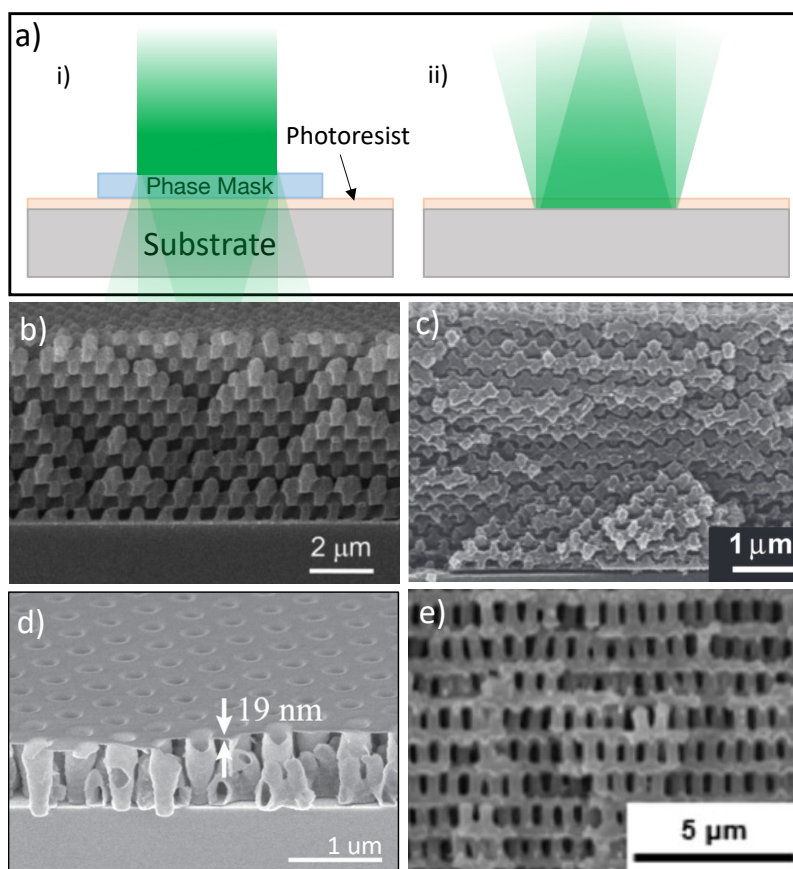


**Figure 2.1:** Holographic lithography and representative products. (a)(i) A single incident laser beam splitting upon passage through a phase-shifting mask, producing an interference region in the photoresist below. (ii) Multiple phase-shifted beams intersecting within a photoresist film. (b-c) Photonic crystals produced via maskless HL.<sup>[116-17]</sup> Both adapted with permission. (d) Nano-patterned metal oxide film produced via HL.<sup>[119]</sup> Reproduced under creative commons license. (e) Cross-section of large area nano-architected material produced via HL.<sup>[120]</sup> Adapted with permission from ref. 20. Copyright 2023 American Chemical Society.

Despite successes in fabricating a variety of geometries, the achievable pattern fidelity is limited by the utilization of phase masks; a major limitation of binary phase masks is the limited control over the generated pattern morphology caused by inherently low diffraction efficiencies, which effectively define the pattern's contrast and morphology. Consequently, producing an open-cell, porous, beam-based, or lattice-like geometry via HL is beyond the capability of current traditional phase mask technology.

## ***2.2 Metasurfaces for Advancing Holographic Lithography***

To overcome the limitation of traditional phase masks, Kamali *et al.* demonstrated via numerical simulation that optical metasurfaces can generate complex 3-dimensional nano-scale distributions of light intensity not achievable with conventional diffractive optics.<sup>[21]</sup> Metasurfaces are comprised of subwavelength features that locally modulate the phase of incoming light, the phase modulation can be polarization selective and therefore complex patterns that are not possible with diffractive masks can be generated under illumination with appropriate polarization components. Kamali *et al.* numerically demonstrated the generation of patterns such as a gyroid, rotated cubic, and diamond which had not been previously been generated via phase-shifting mask.<sup>[21]</sup> Consequently, we hypothesized that a metasurface mask could be designed to achieve lattice-like geometries more amenable to filtration applications among other properties such as increased mechanical resilience to impact. Collaboration with Prof. Andrei Faraon and his research group at Caltech yielded the design and manufacture of a metasurface that numerical simulation suggested would meet our design goals. The metasurface we utilized in this work was composed of an array of 900 nm-spaced face-centered unit cells of five 115 nm-diameter 300 nm-tall crystalline Si nanopillars spaced at  $s = 225$  nm on top of 1 mm-thick quartz substrate. Figure 2.2a contains scanning electron microscopy (SEM) images of a  $3 \times 3$  array of unit cells spaced by distance  $p = 900$  nm (top view) and a zoomed-in view of a single unit cell ( $45^\circ$  tilt view). The utilized mask was hypothesized to generate a near field interference pattern that resembles struts organized in layered 3D brick-and-mortar-like patterns as shown in Figure 2.2b, according to simulation. The light intensity pattern was calculated by finite difference time domain (FDTD) and angular spectrum propagation simulations by our collaborators in the Faraon group. We hypothesized that this mask had sufficient contrast to be applicable in an HL process. This chapter will detail the assessment of our hypotheses and the high-throughput lithography process designed as a result.

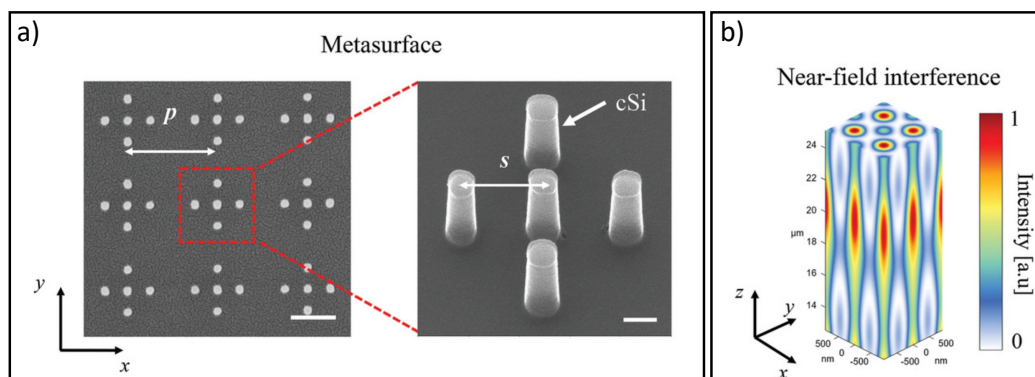


**Figure 2.2:** Metasurface mask and interference pattern. (a) A top-view helium-ion microscopy image of the utilized metasurface (scale bar: 450 nm). Inset represents a zoomed-in tilted micrograph of the outlined region (scale bar: 100 nm). (b) Near-field 3D intensity modulation generated by the metasurface, color represents light intensity normalized by the maximum intensity.

### 2.3 Constitutive Material: SU-8 Photoresist

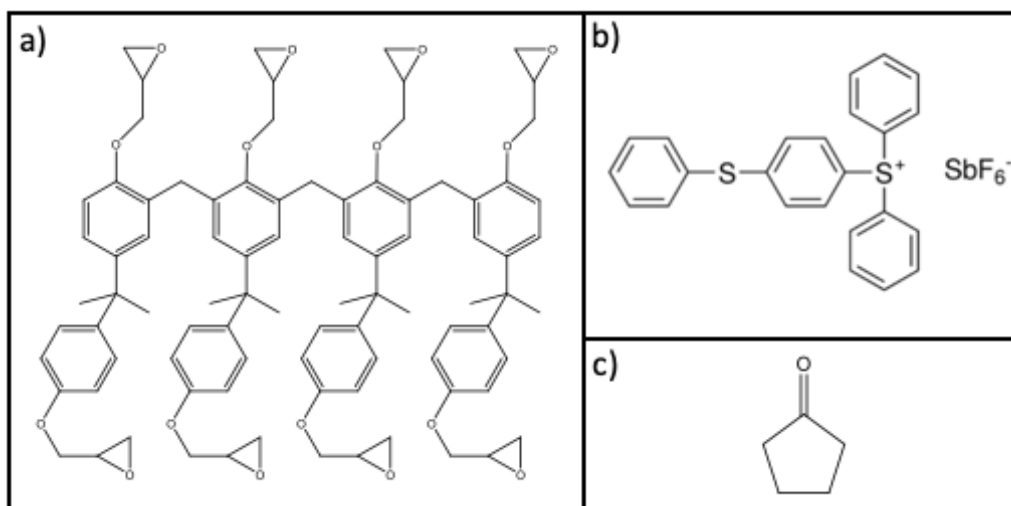


**Figure 2.3:** SU-8 photoresist constituents. (a) A representative oligomer of SU-8, or a 4-unit oligomer of bisphenol A diglycidyl ether. (b) A UV-sensitive triarylsulfonium salt photoacid generator. (c) A highly volatile solvent, cyclopentanone.

For this process, we designed around a commercial photoresist and industry standard, SU-8, the primary constituents of which are outlined in Figure 2.3. The SU-8

monomer participates in cationic ring-opening polymerization of its epoxides initiated by the photoacid produced from the triarylsulfonium salt,<sup>[22-23]</sup> either via direct excitation or abstraction of a radical from another photosensitive compound.<sup>[24]</sup> For visible light sensitization, we used a fluorone dye sensitizer, 5,7-diiodo-3-butoxy-6-fluorone (DIBF, HNu 470) in conjunction with an OPPI diaryliodonium salt (HNu 254). A potential mechanism for this photoacid production is presented in Figure 2.4 below.

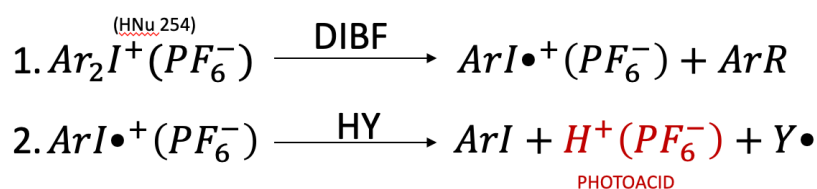


**Figure 2.4:** Visible light photoacid generation. A diaryliodonium salt (HNu 254) abstracts a radical from visible-light irradiated DIBF (HNu 470) and subsequently reacts with a proton donor, most commonly stray photoresist solvent, to produce a strong photoacid (indicated in red) in this two-step mechanism.

The presence and concentration of generated photoacid are linearly correlated to irradiation intensity; therefore, a varied intensity profile such as an interference pattern can be transferred, hence its lithographic functionality. It is important to note the complexity of this system; namely, that it experiences reaction and diffusion of the generated photoacid simultaneously. The high viscosity of the photoresist material suggests that the rate of polymerization is macroscopically diffusion-limited, both of the photoacid and of the polymers as propagation of the living cationic polymerization proceeds.<sup>[25]</sup> Consequently, the temperature and duration of hotplate baking steps are critical to ideal resolution of written features. These phenomena are discussed in greater detail in Chapter 3.

## 2.4 Lithography Method Development

### 2.4.1 Optical Apparatus and Raster Optimization

To fabricate nano-architected materials with macroscopic lateral dimensions as discussed, we designed a laser scanning lithographic system (Figure 2.5). The system is composed of a high-precision XY linear piezo-stage and a 532 nm Verdi V6 solid-state Nd<sup>3+</sup>:YVO<sub>4</sub> laser (Figure 2.5b). The beam is directed orthogonally to the scanning plane of the stage, which rasters the metasurface mask placed in direct contact with the photosensitive material, under the fixed laser beam similarly to Figure 2.1a. This scanning approach is amenable to scalable fabrication of samples with macroscale lateral dimensions because it can easily accommodate a large range of mask dimensions. We optimized the process by controlling the width of the laser beam  $w$ , the stage scanning speed  $v$ , and the scanning step size  $d$  between sequential lines to create a uniformly accumulated exposure dose for a given beam power  $P$ , defined below as Equation 2.1.

$$D = \frac{P}{vd} \quad (2.1)$$

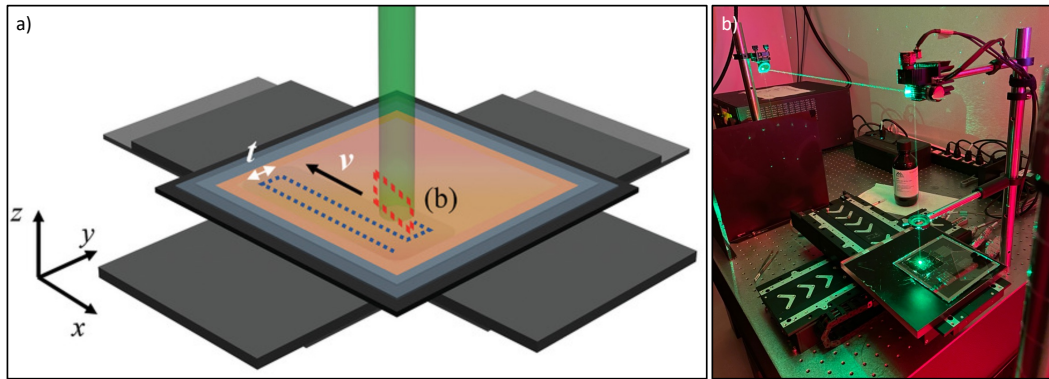


**Figure 2.5:** Metasurface-enabled holographic lithography apparatus. (a) Schematic representation of the lithographic setup. The scanning trajectory of a laser beam is highlighted by the dashed blue line. Note that parameter  $t$  here is represented as  $d$  in Eq. 2.1. (b) A photograph of the lithographic setup. Not photographed are a mechanical shutter and aperture through which the beam passes before being directed above an anodized aluminum barrier. The beam is directed via a galvanometric mirror orthogonally toward the mask surface, under which sits the photoresist material to be

patterned. The stage-substrate and resist-mask interfaces are infilled with an index matching oil to minimize reflections.

To optimize the scanning step size for a given beam size we implemented a numerical simulation that quantifies the uniformity of the deposited dose distribution. We used the TaperCamD-uCD23 beam profiles to record the 2-dimensional beam intensity (Figure 2.6a). From this, the beam width was estimated around 2.14 mm. To simulate the scanning procedure, temporal discretization was applied, therefore the final intensity distribution could be approximated by a sequential summation of Gaussian beams shifted in the horizontal and vertical directions. The horizontal shift was assumed to be  $d$ , the scanning step displacement, and the vertical  $I/v\delta t$ , where  $v$  the scanning speed and  $\delta t$  the temporal step size. To assess the uniformity of the resulting intensity distribution  $I$  we calculate the reverse contrast given by Equation 2.2. A higher value of  $U$  corresponds to a higher uniformity. For our simulation we utilized a time step of 0.1 us and a scanning speed of 1.5 mm/s; the scan step displacement spacing was varied between 0.1 and 1 mm in steps of 0.0091 mm. Due to the sudden drop-off occurring after  $d = 0.5$  mm, a conservative displacement of 0.4 mm was selected to maximize exposure homogeneity.

$$U = 1 - \frac{I_{max} - I_{min}}{I_{max} + I_{min}} \quad (2.2)$$

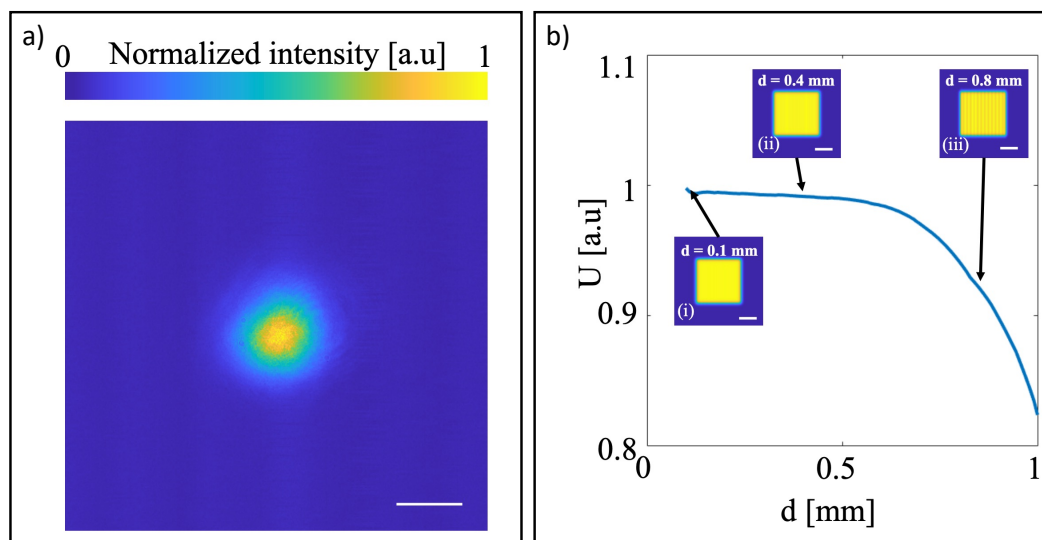


**Figure 2.6:** Raster scan optimization. (a) Recorded beam profile (scale bar 1 mm). (b) Uniformity factor for various beam step sizes. The insets show the resulting intensity distributions at step sizes 0.1 mm, 0.4 mm, and 1 mm, respectively (scale bar 4 mm).

#### 2.4.2 Exposure & Processing Conditions

For our experiments we utilized laser powers in the range of 0.23–0.25 W, the raster scan spacing  $d$  was chosen at 0.4 mm and the scan speed  $v$  was set to 1.5 mm/s which resulted in doses between 0.38 and 0.41 J/mm. The system is utilized to expose 1 mm-thick  $2 \times 2$  in<sup>2</sup> soda-lime glass slides coated with a layer of 30–40  $\mu$ m negative-tone epoxy-based photoresist (SU8 2050) sensitized for 532 nm light with HNu 470 and deposited by spin-coating. We exposed areas of  $3 \times 3$  cm<sup>2</sup> which took a total time of 24 min. Upon laser exposure, photoacid was generated from the onium-salt-based visible-light photosensitizing system at concentrations proportional to exposure intensity. Following exposure, the sample was baked at 65° C for 270 s to promote photoacid and polymer chain diffusion necessary for cationic polymerization of the epoxide rings. Low temperature thermal post-exposure bake doses close to the glass transition temperature ( $T_g$ ) were selected to limit diffusion lengths while maximizing local mobility of chains for polymerization, the time for which was optimized parametrically with final pattern resolution. The photoresist was developed in propylene glycol monomethyl ether acetate (PGMEA) for 2 h, after which it was

washed in isopropanol to remove unreacted SU-8, and then air dried. The exact geometry of the resulting pattern is directly linked to the 3-dimensional light intensity distribution generated by the metasurface.

## ***2.5 Fabrication & Microstructural Characterization***

### ***2.5.1 Results***

Figure 2.7 shows a photograph of a typical 30  $\mu\text{m}$ -thick nano-architected sheet produced via this process patterned over the area of  $2.1 \times 2.4 \text{ cm}^2$  on a glass substrate. The opaque region of the sheet corresponds to the nano-architected material, and the translucent periphery corresponds to the monolithic un-patterned SU-8. The white appearance of the sheet is attributed to its strong scattering over a broad band of visible-light wavelengths. Cross-sectional SEM images demonstrate that the pattern was preserved and successfully developed throughout the thickness of the material (Figure 2.7b), with the resulting architecture of brick-and-mortar arrangements of beams, with each horizontal layer shifted by half a period in both lateral directions respective to the underlying one (Figure 2.7b inset). The SEM images reveal a lateral periodicity of  $900 \pm 10 \text{ nm}$ , which matches the periodicity of the metasurface mask, and a vertical periodicity of  $1.62 \pm 0.02 \mu\text{m}$ , which is 30% lower than the periodicity of  $2.39 \mu\text{m}$  predicted by FDTD simulations (shown in Figure 2.2b). Based on the cross-sectional images at different depths throughout the sample (Figure 2.7c), the beam diameter  $d$  increases by  $\sim 15\%$  from the sample surface to base. The average beam width varied between  $462 \pm 42 \text{ nm}$  in the top layers to  $523 \pm 26 \text{ nm}$  in the bottom layers. The unit cells in the upper 20% of the sample height have a fully open-cell morphology (Figure 2.7c(i)), the unit cells in the center region and below (Figure 2.7c(ii),(iii)) preserve the laterally open-cell morphology but lose the vertical interconnectivity. Based on the measured beam diameters, we estimate that the relative density, or volume fraction, to vary between 0.2 and 0.35 throughout the thickness of the material.

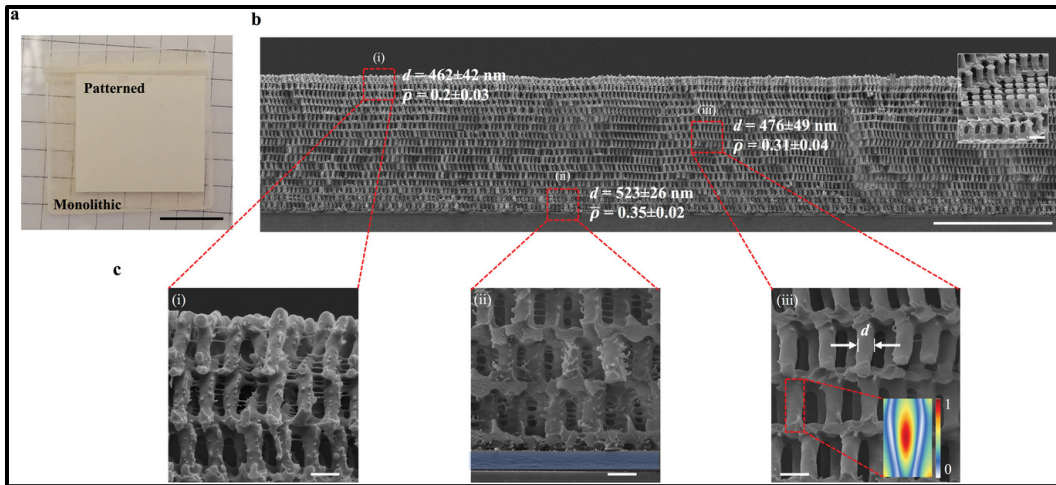


**Figure 2.7:** Morphology and pattern fidelity. (a) A top view photo of the fabricated sample. White square in the middle corresponds to the patterned area, whose appearance is opaque (scale bar: 1 cm). (b) SEM image showing a typical cross section of the fabricated material. A clear pattern transfer is observed throughout the entire sample thickness (scale bar: 25  $\mu\text{m}$ ). The inset shows the beam arrangement within a single layer (scale bar: 1  $\mu\text{m}$ ). (c) A zoomed-in SEM image of the cross section showing the generated beam structure and difference in diameter  $d$ . The blue area in panel (ii) corresponds to the adhesion layer (scale bar: 1  $\mu\text{m}$ ).

### 2.5.2 Discussion

As shown in Figure 2.7a, the white macroscopic appearance of the produced samples indicates strong scattering in the visible wavelength range, an observation in contrast to the expected photonic response from highly ordered structures with periodicity of 900 nm. This observation is consistent with the presence of morphological variations and defects within the sample, especially on the surface. Due to inconsistent SU-8 thickness across the sample, the final unit cell does not always resolve such that the individual beams connect to the horizontal layer. This produces an array of nanopillars on the surface of the sample that cannot support their own weight during development that collapse, producing a non-uniform surface condition that produces non-uniform scattering. Furthermore, examining the cross-sectional SEM images in Figure 2.7 elucidated that although our fabrication method could topologically preserve the unit cell morphology as no collapsed or unexpected structures were observed across the sample, there were still non-negligible morphological variations and discrepancies from the theoretical and numerically expected pattern.

The simulated light intensity (Figure 2.2b) predicts the beams to have a convex shape, i.e., thicker in the center cross section and tapering toward both ends; SEM images in Figure 2.7c demonstrate that they are slightly concave. This discrepancy can be attributed to an optical dose gradient within each beam, where its mid-section experiences a higher optical dose due to the nature of the interference, which causes a greater degree of cross-linking in that region and a concomitant enhanced volumetric shrinkage of SU-8. Higher cross-linking densities result in lower free volume within the polymer which in turn lead to higher volumetric shrinkage.<sup>[26]</sup> The optical dose, and consequent photoacid concentration, relative to the ideal dose determines whether the beams are interconnected and whether the resulting nano-architecture is a closed- or an open-cell cellular solid. If the photoresist is underexposed, the connections between neighboring beams do not fully cross-link and therefore the interconnecting elements of the individual unit cells partially dissolve during development, producing a structure that is weakly or not at all interconnected, leading to structure collapse. If it is overexposed, the pores become fully closed and eventually the structure becomes fully solid as the volume fraction approaches 100%. Our experiments indicate that when the optical dose is sufficiently high to produce closed-pore unit cells, critical point drying is required after the development and washing with isopropanol to retain their shape. Open cell nanoarchitectures remain robust even when dried in air, with no indication of feature collapse (Figure 2.7).

Cross-sectional images convey the presence of slight imperfections in the lattice geometry such as tilted beams with respect to the vertical direction, most likely caused by the significant swelling of the cross-linked polymer network during the long development time of 120 min and the subsequent non-uniform shrinkage that takes place during the washing and drying steps. The longitudinal periodicity of  $1.62 \mu\text{m}$  was also  $\sim 30\%$  less than the theoretical value, which can be attributed to the well-known volumetric shrinkage of SU8 induced by cross linking, reported to be as high as  $40\%$ .<sup>[26-28]</sup> For films attached to a substrate, this shrinkage occurs through

vertical contraction because of the bi-axial lateral constraint imposed by the rigid substrate.<sup>[29]</sup>

The 15% thickening of the beams toward the bottom of the sample (Figure 2.7b) indicates a depth dependent variation of one or more of the following factors: generated light pattern, processing conditions of the photoresists, or solvent content gradient within the photoresist. Given the high transverse coherence of the utilized laser source and the 6 mm-wide laser exposure spot, we expect a uniform 3-dimensional pattern throughout the photoresist thickness. During photoresist processing, the existence of both thermal and chemical gradients cannot be excluded. Cross-linking of the photoresist is achieved by a post exposure bake on a hot plate; this could result in an increased temperature gradient toward the bottom of the sample. If we consider the bottom of the sample to maintain a conductive boundary condition at 65 °C and the top of the sample to maintain a convective boundary condition closer to ambient temperatures (~17-19 °C), a considerable temperature gradient is to be expected. While the air above the hotplate and consequently the sample increases as the bake step proceeds, even a difference of 5 °C could have drastic effects on polymerization conditions, since baking temperatures are near the  $T_g$  of SU-8, which is reported to be 55-60 °C for un-polymerized material.<sup>[30]</sup> A higher temperature at the bottom would result in higher photoacid and polymer chain diffusive mobility, and consequently wider beams. We did not quantify the thermal gradient in this work; our analysis of the process indicates that the ambient heating conditions during post-exposure bake are crucial in defining final sample morphology.

Another factor that determines the mobility of the photoacid and the sensitivity of the photoresist is the remaining solvent after the pre-exposure soft bake of the photoresist.<sup>[31-32]</sup> Thick photoresist layers are well known to develop solvent gradients due to limited solvent diffusion at the surface of the photoresist.<sup>[33]</sup> An increase in remaining solvent towards the bottom at the photoresist leads to an increased

photoacid diffusion length and, similarly to the temperature gradient, to an increased beam width at the bottom. This is further compounded by the onium salt photo-acid generator mechanism, which requires solvent as a proton donor to produce the acid, as shown in Figure 2.3. Greater concentrations of solvent yield higher sensitivity photoresist due to greater availability of proton donors,<sup>[23]</sup> which further contributes to the thickening of the lateral beam dimension. We therefore conclude that the change in pattern morphology is a combination of effects from both thermal and solvent gradients through the thick photoresist.

## ***2.6 Experimental Methods***

*Sample Preparation:* Soda-lime glass microscope slides (1 mm thick and 2 x 2 in) were utilized. The first step of substrate preparation was to produce an adhesion-promoting layer on the glass. After the glass slides were cleaned in acetone and isopropanol baths, 1 mL of SU-8 2000.5 (Kayaku Advanced Materials) was spun at 2000 rpm for 30 s, followed by a 10 min pre-exposure bake at 85 °C, 10 min UV exposure, and a 20 min post-exposure bake at 85 °C, yielding a glass substrate optimized for photoresist adhesion. Prior to application of the SU-8 layer for patterning, the photoresist must be sensitized to the operating wavelength. To that end, a visible light sensitizing system, HNu 470 and HNu 254 (Spectra Group Ltd), was added such that the ratios to SU-8 solids were 0.53% and 4.66%, respectively, in a 70% solids resist, all by mass. Sensitized SU-8 was spun onto substrates with adhesion layers at 3000 rpm for 30 s to produce ~40  $\mu\text{m}$  uniform coatings. The sample was then baked at 65 °C for 10 min, then at 95 °C for 30 min.

*Photoresist Exposure:* Glass slides prepared with solid SU-8 films were placed on an acrylic block coated in Acktar black film and an index matching mineral oil to minimize internal reflection at interfaces. The acrylic block itself was affixed to a Physik Instrumente XY-translation stage. Index matching mineral oil was then deposited directly onto the SU-8, and the mask was placed, feature-side down, on the sample. Gentle pressure was applied to ensure that the sample and mask planes were

parallel, with no trapped gaps. The laser was then set to exposure power (230–270 mW) and allowed to stabilize for 75 s while blocked by an external shutter. The shutter was then opened, and the translation stage raster scanned the sample at 1.5 mm/s relative to the stationary beam, displacing each line scanned by 0.4 mm.

*Post-Exposure Processing:* After exposure, samples were baked at 65 °C for 3.5 min, at which point the hotplate was turned off and the sample rested as the hotplate cooled for another 10 min. The sample was then placed suspended and inverted in a bath of propylene glycol monomethyl ether acetate (PGMEA) for 2 h for development. The samples were then washed in a series of baths to perform a solvent exchange from PGMEA to isopropanol. After ~1 h in 100% IPA, samples were air dried.

*Volume Fraction Estimation:* Cross-sectional scanning electron images were utilized to estimate the volume fraction at various depths. The beam pillar widths and interlayer thicknesses were measured at the top, center and bottom of the cross-sectional image shown in Figure 2.6b. Under the assumption that each unit cell comprises in total four quarter beams and two halves of the interlayer plates, the volume fraction was estimated.

## ***2.7 Summary & Outlook***

In this chapter, we successfully proved that phase-shifting metasurface masks designed by our collaborators in the Faraon lab can produce interference patterns of sufficient contrast for application to holographic lithography. Consequently, we successfully designed and implemented a novel approach to visible light HL, utilizing a nano-precise XY-translation stage to linearly raster scan the mask at a 0.4 mm offset with the unmodified Gaussian laser beam operating at 532 nm. We demonstrated that by utilizing this technique with a nominal laser power of 230-270 mW, we were able to resolve ~500 nm features in a brick-and-mortar lattice-like geometry in visible light sensitized SU-8 negative tone photoresist with a 900 nm lateral period to match the periodicity of the metasurface mask. Vertical periodicity

exhibited reduction in dimension from expected pattern, likely due to characteristic volumetric shrinkage of constituent photoresist. Furthermore, inhomogeneities in beam shape and diameter elucidated depth dependent resist sensitivity that, while not characterized directly, have clear implications for thick resist film materials manufacturing and development. These successes contribute to the rapidly growing field of nano-architected materials manufacture at scale and provide a largely unexplored pathway to commercialization of nano-architecture-enabled phenomena.

While the materials produced via this technique were evaluated for their high impact resilience and promising mechanical properties in the adapted publication, these tests and experiments are beyond the scope of this thesis. My contributions to this project were in service of developing a process and resultant material amenable to filtration applications, and it is abundantly clear from the reported results that said material leaves much to be desired, and the shortcomings can be examined as either rooted in the technique or in the constituent material, SU-8. Regarding the former, we can identify a single contributing factor: the absence of a homogeneous open pore geometry. While we had hoped that the metasurface presented in Figure 2.2 would produce an open geometry, it is clear from generated materials that due to inhomogeneities in mask diffraction efficiency, local dose inhomogeneity, or simply due to the vertical resist sensitivity variation, materials produced are not uniformly fully open cells, which would inhibit inert fluid flow in those regions. To produce materials better suited for homogeneous flux, a more consistent metasurface mask is necessary that can produce uniformly open-cell geometries.

SU-8 proved to be a poor material selection for applications in water filtration due first to its poor wettability; in literature it is considered hydrophobic despite its reported contact angle of  $\sim 80^\circ$ ,<sup>[34]</sup> which macroscopically results in resistive forces originating from surface tension when passing water through a hypothetically open-pore structure. Furthermore, we observed consistent mechanical deformations of produced films upon delamination of samples from glass substrates, wherein samples

curled inward to form a macroscopic tubular structure, as shown in Figure 2.8. We suspect that this curvature is the result of latent mismatch stress between the photoresist and substrate due to the observed volumetric shrinkage of SU-8 of 30-40%, depending on cross-link density and epoxide conversion.<sup>[26-28]</sup> With a static boundary condition at the photoresist-substrate interface, the sample cannot shrink isotropically, resulting in energy storage via a radially oriented stress profile within the SU-8 opposed by adhesive forces keeping the film in place. Upon sample delamination, the energy is released as the sample curls. This effect is compounded by variations in cross-linking density throughout the thickness of the film.<sup>[35]</sup> These shortcomings, alongside additional design considerations, directly informed the development of a new photoresist as a substitute for SU-8 that would produce materials more amenable to water filtration and surface functionalization, to be detailed in the subsequent chapter.

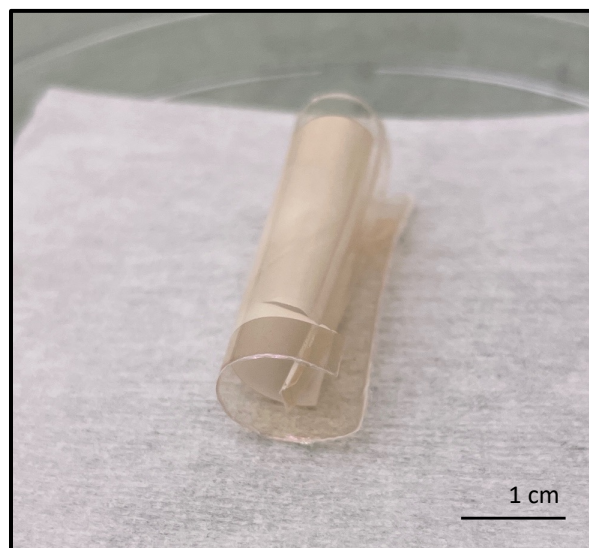


**Figure 2.8:** SU-8 film curling. Delaminated films manufactured via our scalable HL technique often curl into tube-like conformations due to residual stresses within the film derived from non-uniform shrinkage and cross-link density.

*Chapter 3***CUSTOM EPOXIDE-BASED FUNCTIONALIZABLE  
PHOTORESIST*****3.1 Photoresist Classification & Mechanisms***

Resists are a class of materials that change aspects of their chemical functionality and solubility in certain developing solvents when exposed to various forms of radiation including beam/lamp sources of electrons, ions, and/or photons; light-sensitive resists are known as photoresists. Those that become more soluble due to exposure are dubbed positive-tone due to the relationship between the final pattern and the mask, and the primary mechanism they are designed around is photodecomposition of a functional group on the constituent material. Commonly used positive-tone photoresists consist primarily of diazonaphthoquinone (DNQ) derivatives dissolved in a non-polar solvent alongside a mixture of high and low molecular weight novolac resin polymers. Upon UV irradiation, DNQ decomposes via release of nitrogen gas into a significantly more polar carboxylic acid and a similarly polar phenol-formaldehyde derivative, both of which are far more soluble in an aqueous base developer than DNQ itself is.<sup>[21]</sup> Additionally, it is believed that DNQ undergoes an azo-coupling between its amino group and the methylene bridges on the novolac resin to increase its molecular weight and further inhibit dissolution in developer solutions.<sup>[37]</sup> There are some positive tone photoresists that rely on polymer chain scission resulting from ion/electron-beam exposure-initiated radical formation at the quaternary carbon center; the most common example of this type of resist is poly(methyl methacrylate).<sup>[38-39]</sup> While the chemistry and functionality of positive-tone photoresist are important for comparative purposes, this thesis will exclusively focus on the alternative: negative-tone photoresist.

Photoresists that become less soluble due to exposure are categorized as negative-tone (i.e., they result in a negative image of the utilized mask) and typically rely on photoinitiated polymerization of the primary constituent material, either a reactive monomer or a low molecular weight telechelic polymer chain. The overwhelming majority of polymer-based negative-tone photoresists fall into one of two categories: free-radical initiated or photo-acid catalyzed polymerization schemes. The former traditionally relies on vinyl-containing monomers such as acrylates and methacrylates that, after homolytic fragmentation of a light-sensitive initiating compound, react with and produce a propagating radical on the growing chain to facilitate polymerization. As the polymer chain rapidly grows, the propagating radical is terminated via several potential mechanisms including peroxy-radical formation upon reaction with oxygen gas in air, radical recombination of propagating chains, radical disproportionation between chains, or radical chain transfer.<sup>[40]</sup> This rapid termination allows for minimal cross-linking between chains in unexposed regions maintaining relatively low molecular weight, while high degrees of cross-linking occur in exposed regions, vastly increasing molecular weight. The smaller molecules then are dissolved in an organic developer solvent, while the larger molecules that are interconnected via cross-links remain insoluble.<sup>[41]</sup> The advent of click chemistry brought a mechanically unique type of radical-initiated resist: thiol-ene systems. Via anti-Markovnikov addition, a thiyl radical attacks an alkene, transferring the radical to the chain, which then interacts with a separate thiol via chain transfer, regenerating the thiyl radical.<sup>[42]</sup> These systems tend to be air insensitive as the formation of peroxy radicals is unfavorable, and therefore termination is primarily the result of radical recombination.<sup>[43]</sup>

The second type of negative-tone photoresist and the focus of this chapter is the photo-acid catalyzed photoresist, the best known of which is SU-8. The overwhelming majority of photoresists within this class consist of telechelic monomers or oligomers terminated by an oxirane, or epoxide ring. The smallest of the cyclic ethers, epoxides exhibit a triangular molecular bond structure, yielding

high ring strain on its tetrahedrally hybridized atoms. Consequently, the epoxide moiety is known for its high volatility and reactivity, capable of experiencing both nucleophilic and electrophilic attacks.<sup>[44]</sup> A single epoxide undergoes a cationic ring opening when the oxygen atom is protonated by nearby generated photo-acid, increasing its net charge. To compensate, an electron is stripped from the more substituted carbon in the epoxide, forming a carbocation that can then attack another epoxide (Figure 3.1). Unlike the radical mechanisms discussed above, cationic ring opening polymerization is a type of living polymerization, meaning that there is no mechanism for reaction termination without direct intervention (by stabilizing the carbocation through a different chemical means).<sup>[45]</sup> Consequently, for an epoxide-based photoresist to resolve programmed features and avoid polymerization in unexposed regions, the photoresist is processed in solid phase to impose a diffusion limitation on polymerization rate.<sup>[46]</sup> This approach necessitates unique processing steps at elevated temperatures to reduce solvent content and increase photoacid/polymer diffusivity that will be further explained in Section 3.3. All future references to “photoresist” will be limited exclusively to epoxide-based systems.

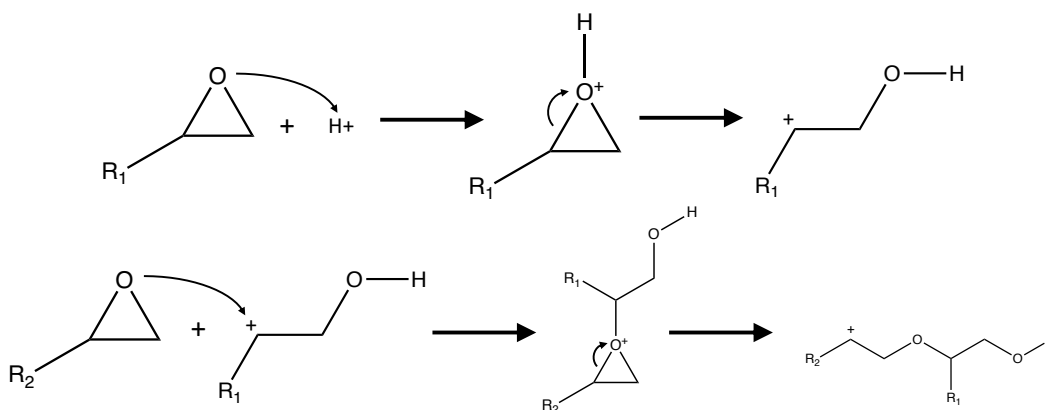


**Figure 3.1:** Acid-catalyzed cationic ring-opening polymerization. A free proton liberated by a photo-acid protonates an epoxide, destabilizing the cyclic ester and producing a carbocation on the more substituted carbon. This carbocation can then interact with another epoxide, and the process repeats, producing a growing polymer via propagating chain growth.

### 3.2 Custom Photoresist Monomer Selection & Design Goals

In the previous chapter, we ultimately concluded that SU-8, despite its ubiquity in literature and industry, was unsuitable for producing materials for use in water filtering applications. We found that film deformation caused by high volumetric shrinkage during cross-linking, relative hydrophobicity, and limited control over both surface and bulk functionalization necessitated the design a custom photoresist for water filtration applications. To address the first two considerations, glycidyl methacrylate (Figure 3.2) was selected as the ideal constituent monomer to build our new photoresist.

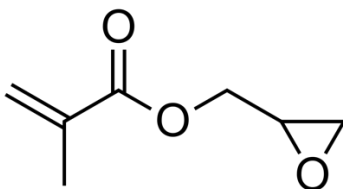


**Figure 3.2:** Glycidyl methacrylate monomer. An ester of methacrylic acid and glycidol, this ditelechelic monomer is well suited to serve as both a chain-builder and a cross-linker.

Glycidyl methacrylate (GMA) has been demonstrated in literature to serve as an ideal basis for custom epoxide-based photoresists due to its ditelechelic nature. For example, after pre-polymerization of the methacrylate, linear homopolymer polyGMA (PGMA) was dissolved alongside a photoacid generator to produce a photoresist that, when subjected to UV exposures via interference lithography, produced patterns structurally indistinguishable from those produced via the same technique with SU-8<sup>[47]</sup>. In that same study by A. Hayek *et al.*, volumetric shrinkage was examined by examining unit cell dimensions of produced samples, and it was shown that while SU-8 exhibited shrinkage of up to 42%, PGMA-based photoresists saw only 6% shrinkage.<sup>[47]</sup> This was hypothesized to be due to the steric hindrance to close packing that SU-8 monomers experience when compared to the flexible carbon-carbon backbone of a poly(methacrylate). Subsequent studies have shown

that the methacrylate of GMA can be easily co-polymerized with other acrylates, methacrylates, and vinyl containing groups to produce co-polymer photoresists with additional useful properties such as high optical transparency,<sup>[48]</sup> cross-linkable nanoparticles<sup>[49]</sup>, and polymer phase-separation.<sup>[50]</sup> While still considered to be largely hydrophobic, GMA-based co-polymers have been demonstrated to be considerably more hydrophilic than the base material, all of which have lower contact angles ( $\geq 70^\circ$ ) than SU-8.<sup>[51]</sup> Consequently, it was hypothesized that materials more amenable to application in water filtration could be manufactured via the development of a novel GMA co-polymer-based photoresist exhibiting the following characteristics:

1. Minimal bulk deformation due to shrinkage
2. Increased hydrophilicity compared to SU-8
3. Facile control of surface functionality

This chapter will discuss the design, synthesis, optimization, and lithographic performance of the photoresist in accordance with those design goals, while Chapter 4 will assess the viability of the produced material as a chemically selective water filtration platform and will address the success with which the design goals were achieved.

### ***3.3 Photoresist Processing***

To sufficiently contextualize the processing optimization and photoresist design explained within this chapter, it is important to understand the methods by which epoxide-based photoresists are properly handled during a lithographic technique such as holographic lithography (Figure 3.3).

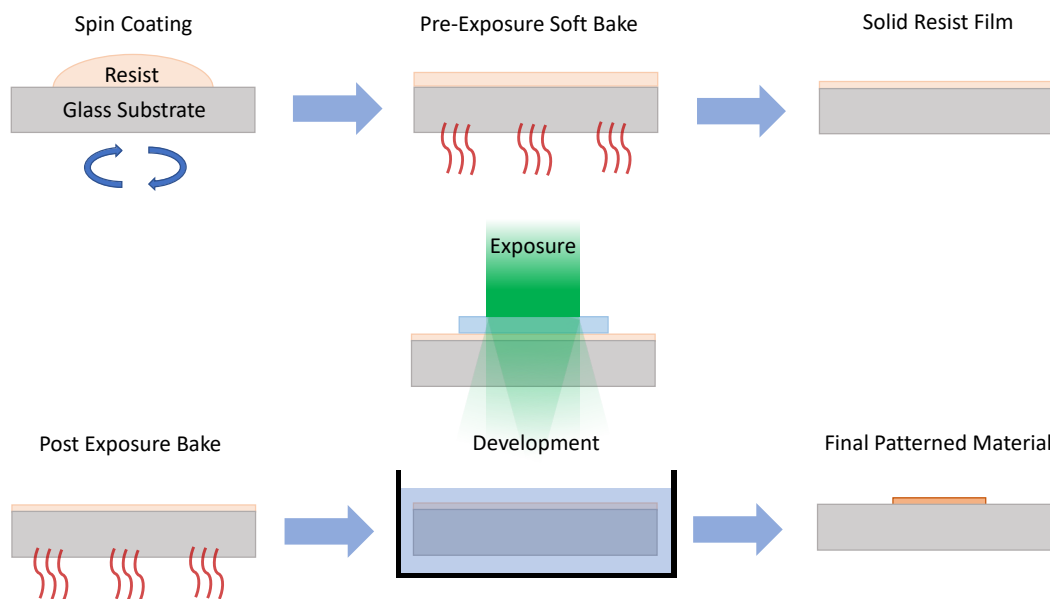


**Figure 3.3:** Epoxide-based photoresist processing steps. Liquid photoresist is spin-coated onto a substrate which is then baked to remove solvent to produce a solid resist film. The sample is exposed, and subsequently baked once again to facilitate diffusion-limited polymerization. The photoresist is then placed in a developer solvent bath to remove unexposed resist and subsequently air dried, resulting in the final patterned material.

*Spin-Coating:* Liquid photoresist is pipetted or poured onto the center of a desired substrate, usually a symmetrical glass or silicon, which is locked in place. The substrate is then rotated at rates between 500 – 10000 rpm, causing the film to spread due to inertial forces, until it begins to spin off the edge of the substrate. The no-slip boundary condition for fluid flow at the substrate interface allows inertial forces to equilibrate with the centrifugal forces driving photoresist radially outwards, yielding a uniform thickness distribution.<sup>[52]</sup> Film thickness has been determined experimentally to scale with solute concentration and resist kinematic viscosity and inversely with spin angular velocity and resist density.<sup>[53]</sup> Consequently, more viscous and concentrated resists spun at slower velocities will result in thicker films. For highly concentrated photoresist solutions (>50% solute by mass) spun at slower rates, solvent evaporation rate is important to consider as well, as for more viscous systems considerable build up in the form of an edge bead occurs along the edges of the substrate, primarily due to surface tension and viscous forces.<sup>[53-54]</sup>

*Pre-Exposure Soft Bake:* A substrate that has been coated with a thin film of resist is then baked to remove solvent. This is typically done on a hotplate to drive solvent upwards and away from the substrate, instead of in an oven where solvent evaporation will occur at the resist surface, trapping solvent beneath low permeability layers. As was mentioned in Section 3.1, solvent content must be reduced to limit diffusivity of polymer chains and generated photoacid to enable resolution of features and limit polymerization to exposed regions. From the Stokes-Einstein equation, we know that diffusivity is a function of the inverse of viscosity, so increasing the viscosity via solvent loss linearly reduces diffusivity. Additionally, reducing solvent content reduces sensitivity of the resist, both by limiting diffusion and by reducing available proton donors for photoacid generation, per the mechanism in Figure 3.1.<sup>[22-23]</sup> Solid resist films are a necessity when performing lithography that requires contact with a mask to prevent contamination or damaging of the resist film.

*Exposure:* A photoacid distribution is generated in the resist film via irradiation from a light source, typically a collimated source such as a laser. In single photon excitation systems, radical generation is linearly correlated to exposure dose according to the sensitizer's quantum efficiency, and under the circumstances employed in the system described in Chapter 2, the radical generates a photoacid at a specific efficiency defined by its reaction kinetics.<sup>[24]</sup> Since the photoacid generator concentration is assumed to be homogeneously distributed throughout the film, we can therefore assume that photoacid generation is linearly a function of cumulative energetic dose deposited per area. This cumulative dose is both a function of the nominal exposure dose as well as the raster scan speed. Instantaneous exposure dose, or the energy delivered per unit area *per time* has secondary effects, primarily local generation of heat for sufficiently high doses, and while this was not explicitly controlled for in this study, the effect contributed to results to be described. Peripheral factors affecting exposure such as internal reflections, laser beam incident angle, and exposure homogeneity are systematically controlled by the technique described in Chapter 2, and consequently will not be discussed at length.

*Post-Exposure Bake:* With a photoacid distribution generated and effectively locked in place in the low mobility solid resist film, it is then returned to the hotplate. As temperature increases, so too does the mobility of the photoacid and polymer chains. Literature suggests that increasing the temperature to just above the resist's uncross-linked glass transition temperature ( $T_g$ ) is ideal for maximizing resolution, allowing polymerization to occur only in exposed regions. As polymerization occurs, molecular weight increases thereby increasing the  $T_g$  of the polymer, effectively terminating the living cationic polymerization via diffusion limitation. Increasing temperature and time have the effect of decreasing feature resolution as diffusion occurs more rapidly and for longer, respectively.<sup>[55]</sup> Additionally, it has been observed that longer and higher temperature bakes tend to result in films with higher strength and elastic modulus, while also developing a more brittle character, which is consistent with the development of a more thoroughly cross-linked polymer network. A wide variety of techniques for post-exposure bake steps exist at varying temperatures and times for just SU-8, many of which result in successful resolution of sub-micron features, indicating that there is not necessarily a single correct set of ideal conditions.<sup>[56]</sup>

*Development:* An exposed and baked sample is then placed in a solvent bath, in which unreacted photoresist oligomers are soluble and consequently are removed from the substrate while the large, cross-linked photoresist molecules are unaffected and remain behind. This process is primarily governed by diffusion of solvent into the film and the resultant counter-diffusion of unreacted material out of the film. Therefore, ideal development time is tied to resist film thickness and the operating temperature, lengthening or shortening the optimal development time, respectively. Insufficient development time often leaves photoresist residues of incompletely dissolved material, reducing resolution of features. Literature suggests that the cross-linking of polymer-based photoresists reduces diffusivity of both developer and photoresist, making resolving encapsulated structures considerably more difficult, while excess development time will induce swelling of cross-linked materials that

manifests as shrinkage stresses during drying steps; this shrinkage effect, however, is still most notably observed due to the pre- and post-exposure bakes.<sup>[57]</sup>

### ***3.4 Surface Functionalization***

While GMA-based photoresists have been demonstrated to exhibit low volumetric shrinkage in literature, the remaining two design goals listed in Section 3.2 are not sufficiently met by a GMA homo-polymer based system. GMA has been noted to be hydrophilic than SU-8,<sup>[51]</sup> but further increasing that hydrophilicity is highly desirable for water-filtering applications. Additionally, to produce water filters capable of targeting specific analytes within an aqueous medium required modification of surface conditions to do so. We hypothesized that by applying appropriate surface modification techniques, the second and third design goals could be satisfied simultaneously.

Traditional approaches to epoxide-based photoresist surface functionalization rely heavily on the presence of primary alcohols and unreacted epoxides as points of attachment for functional groups and molecules capable of affinity-based captures. For example, Blagoi *et al.* demonstrated that opening unreacted epoxides on an SU-8 substrate with cerium ammonium nitrate produced hydroxyl groups and then silanizing with aminosilane produced a pendant primary amine affixed to the surface capable of protein binding.<sup>[58]</sup> Similarly, Aekbote *et al.* demonstrated that primary amines produced by the aminosilanization technique could be used both as a substrate for covalent biotinylation and as a means of electrostatically capturing negatively charged Au nanoparticles when substrates were treated with acid.<sup>[59]</sup> Another example from Anbumani *et al.* sees the hydroxyl groups further oxidized to carboxylates via oxygen plasma treatment which then form NHS-esters with N-hydroxysuccinimide, yielding a surface capable of non-specific reaction with the amine N-terminus of a protein.<sup>[60]</sup> As yet another example, via what they called a “nitrene insertion” technique, Nagaiyanallur *et al.* demonstrated that amine-

terminated polymers could be grafted to SU-8 surfaces via non-specific azide degradation, yielding pendant amines for further functionalization purposes.<sup>[61]</sup> This list of examples is not exhaustive, but serves to illustrate the variety of potential methods for surface functionalization of epoxide resists. While it is reasonable to hypothesize that these techniques are applicable to a PGMA homo-polymer photoresist, there are several drawbacks that ultimately led to exploring an alternative method. The first two techniques rely on full surface treatments and does not allow for partial, or local surface functionalization; an entire sample must be treated at once. Additionally, the density of surface functionalization is only controlled by the absence or presence of hydroxyl groups, which itself is a function of the epoxide oxidation kinetics and the degree of cross-linking within the SU-8 sample, both affording limited control. The third technique, while producing surfaces with localizable and density-controlled functionalization sites, relies on the grafting of commercially unavailable and specific polymer products that are the result of entirely separate complex synthetic, polymerization, and purification steps.

To circumvent these limitations and produce a unique and facile surface functionalization mechanism, we elected to create a PGMA-based co-polymer that incorporated a protected amine to the photoresist such that, after lithographic processing and development, primary amines could be liberated via a simple 1-step deprotection to engage in subsequent surface reactions. Amine protection is necessary to avoid undesirable side reaction between the amines and present electrophiles, such as an epoxide in a photoresist. The overwhelming majority of amine protecting groups, such as t-BOC and FMOC, are chemically sensitive and often specifically pH sensitive,<sup>[62-65]</sup> which is undesirable for incorporation in a photoresist due to the reactive radicals and photoacids produced during resist processing steps. We therefore synthesized and utilized a photo-labile amine protecting group derived from UV-sensitive *o*-nitrobenzyl alcohol, which was reported to be chemically inert with respect to both radicals and pH changes, as well as thermally stable up to 110 °C.<sup>[66]</sup> This methacrylate monomer, known as 2-

{[(benzyloxy)carbonyl]amino}ethyl 2-methylprop-2-enoate (ONBAMA) is the product of a facile condensation synthesis between *o*-nitrobenzyl alcohol and 2-isocyanatoethyl methacrylate (Figure 3.4). Successful synthesis of ONBAMA was confirmed via  $^1\text{H}$  NMR (Figure 3.5). We hypothesized that a random co-polymer of GMA and ONBAMA, to be now referred to as poly(GMA-*rand*-ONBAMA) (PGRO), could serve as an epoxide-based photoresist capable of localized and facile post-processing functionalization. We additionally hypothesized that, due to its constituent monomers, this photoresist material would be considerably more hydrophilic than structures produced in SU-8.

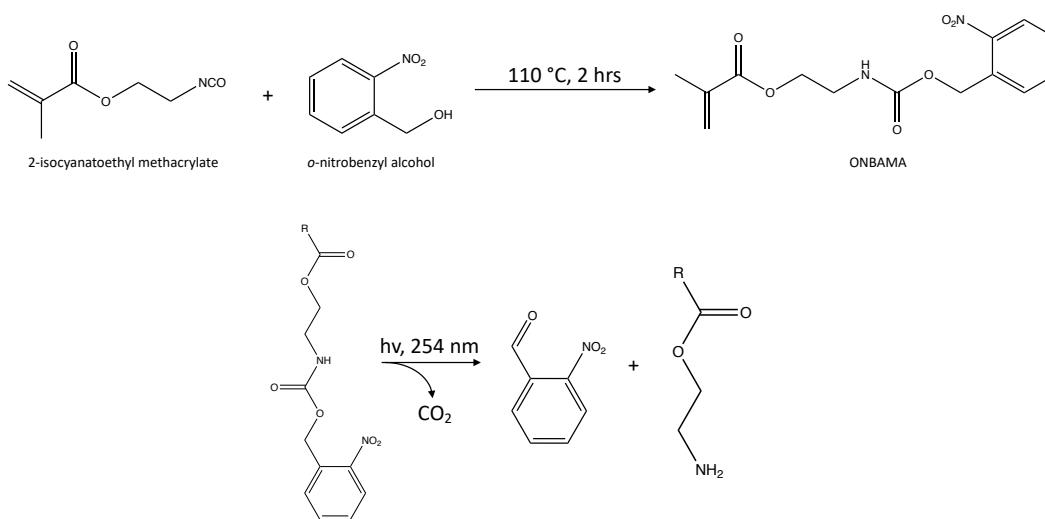


**Figure 3.4:** ONBAMA synthesis and deprotection. Reaction between the isothiocyanate and the alcohol forms a UV-sensitive but chemically inert carbamate. Upon irradiation with UV-C light, the carbamate decomposes, releasing carbon dioxide gas, a yellow-brown colored aldehyde, and the desired primary amine, still affixed to its initial substrate (R).

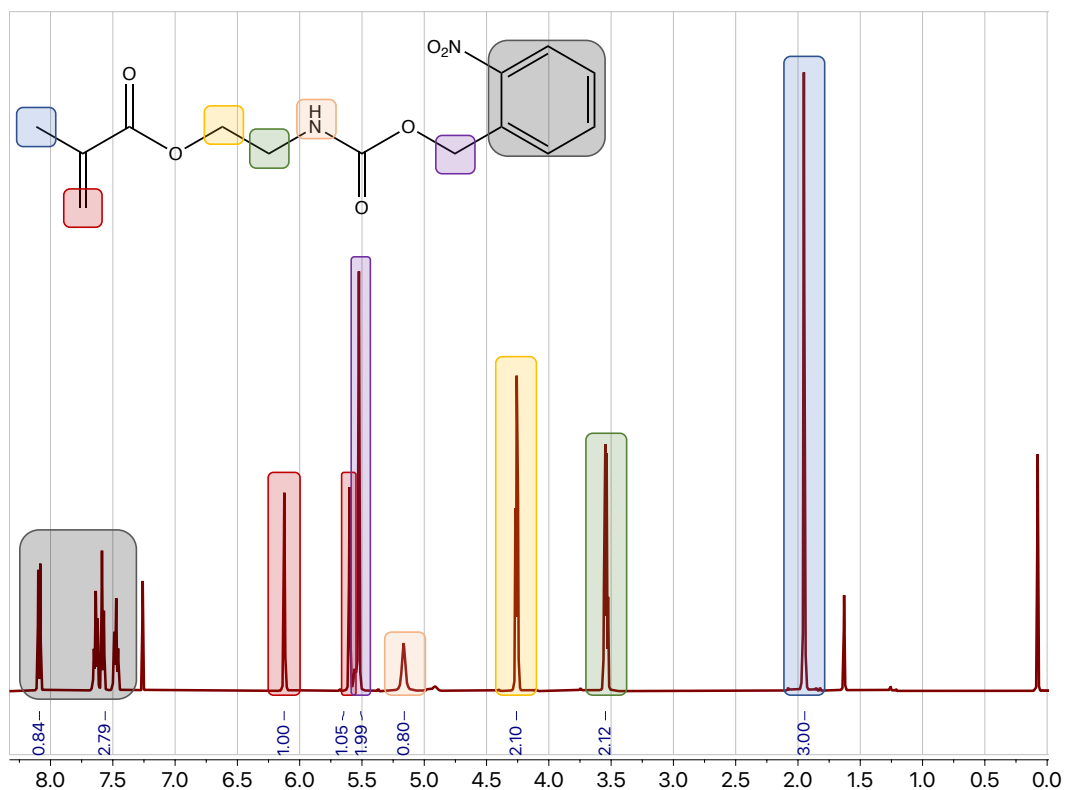


**Figure 3.5:** Synthesized ONBAMA  $^1\text{H}$  NMR. Peaks correspond to hydrogen atoms present on corresponding boxed atomic centers. The two hydrogen atoms on purple center ( $\delta = 5.52$ ) can be used to identify the presence of ONBAMA in co-polymers, while the two hydrogens on the red center ( $\delta = 5.57, 6.15$ ) can be used to identify reaction conversion and the presence of unreacted monomers during radical polymerizations. Integrations and chemical shifts agree well with literature references.<sup>[66]</sup>

### 3.5 Photoresist Formulation & Pre-Polymer Synthesis

A photoresist consists of a multifunctional solid phase linear polymer or small monomer dissolved in a solvent alongside a photoacid generator; the obvious tunable parameters are therefore the relative concentrations of these elements. SU-8 being a model system, we elected to utilize the same solvent, cyclopentanone, as it exhibited good solubility of GMA polymers and had been used previously in literature examples of PGMA photoresist.<sup>[47, 49]</sup> We elected to utilize nearly the same concentrations of HNu 254 & HNu 470 photoacid generator and visible light sensitizer as was used in our sensitized SU-8 to afford a basis for comparison between the two systems. What remained was the concentration of polymer, which we

realized we simply needed to maximize. Because our primary motivation was the manufacture of films for filtration, or more specifically, a structure that will be subjected to pressure differential, we wanted to produce the most robust film possible. This required the thickest possible films to be deposited via spin-coating, the thickness of which is proportional the photoresist's viscosity, which increases with polymer concentration. Previous work on GMA-based photoresists suggests that polymer solubility decreases non-linearly with molecular weight,<sup>[47]</sup> indicating that the shortest chains were most desirable.

To produce short linear polymers with pendant epoxides as an analog to SU-8 to serve as the backbone of the photoresist, two potential polymerization schemes were identified: free radical polymerization (FRP), and atom-transfer radical polymerization (ATRP). FRP is advantageous in that it is simple to establish and troubleshoot, produces polymer product rapidly, and requires nothing more than an inert atmosphere, a solvent, monomers, and an initiator; however due to its simplicity and reaction rate, little control is afforded to both the length/molecular weight and the polydispersity of the polymer products. ATRP, on the other hand, is a controlled polymerization scheme that, while slower and more complex (requiring more reagents, purification, separation schemes), is capable of precise control over polymer size and molecular weight. To determine the ideal technique, PGMA homopolymer were synthesized via thermal FRP (Figure 3.6) and via initiators for continuous activator regeneration (ICAR) ATRP<sup>[57]</sup> to determine ideal conditions, and PGRO polymers were then produced at those conditions at an 85:15 respective ratio, producing polymers with  $M_n = 10\text{--}30$  kDa, which is well within acceptable and reported ranges for GMA-based photoresists.<sup>[47-50]</sup> Resulting polymers were analyzed via <sup>1</sup>H NMR and gel permeation chromatography (GPC) to verify synthesis, composition, and molecular weight ( $M_n$  &  $M_w$ ). Ultimately, FRP was selected as the ideal mechanism due to the ease with which large volumes of high-purity polymers could be produced, as ATRP presented difficulties with both purity and scale-up.

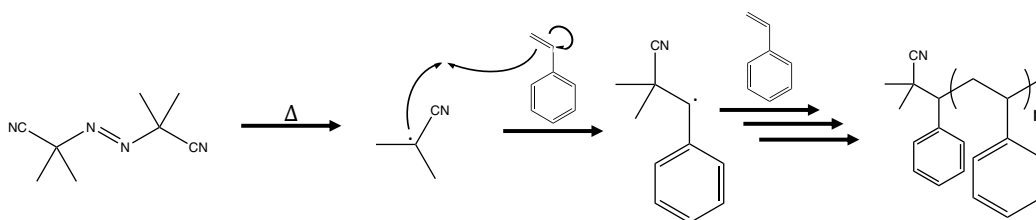


**Figure 3.6:** Free radical polymerization mechanism of styrene. Azobisisobutyronitrile (AIBN) undergoes homolytic fragmentation when heated past its decomposition temperature, producing radicals that attack carbon-carbon double bonds in vinyl monomers, yielding a new radical on the monomer. Once initiated, the radical attacks additional monomers, growing the chain until the polymerization is terminated via radical recombination or disproportionation.

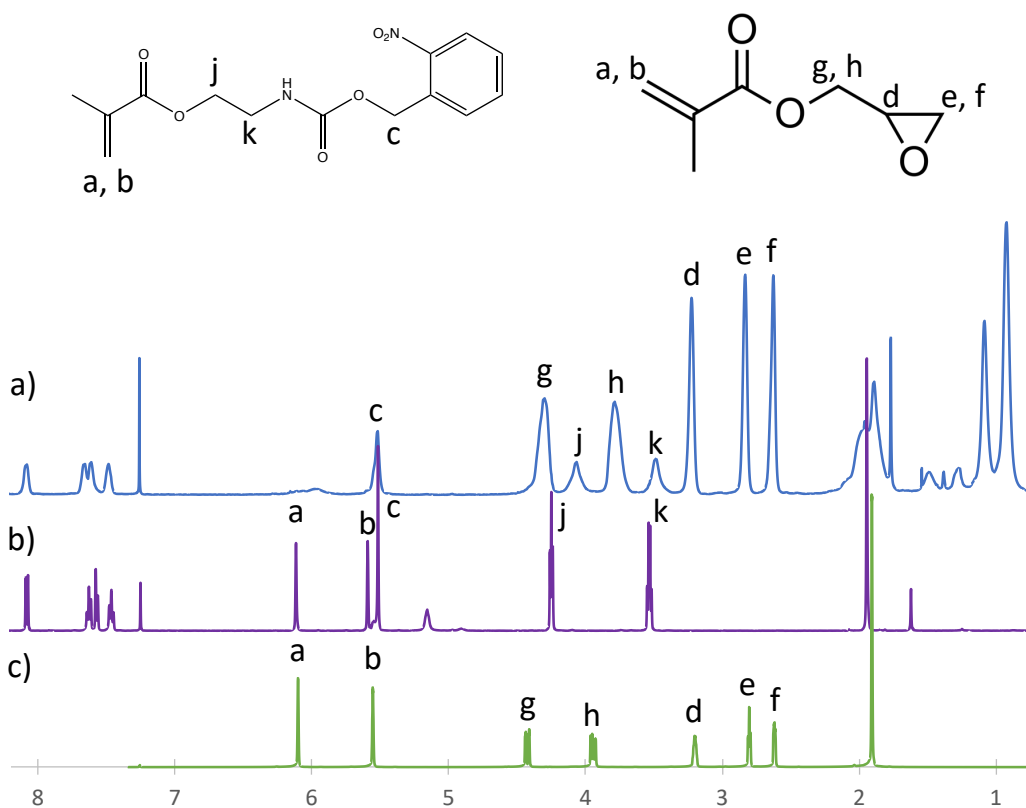


**Figure 3.7:** Co-polymer <sup>1</sup>H NMR. NMR spectra for (a) PGRO produced via FRP, (b) synthesized ONBAMA monomer, and (c) purchased GMA monomer.

Peak	Normalized Integration
c ( $\delta = 5.30 - 5.70$ )	1.00
d ( $\delta = 3.10 - 3.33$ )	2.97
e ( $\delta = 2.75 - 2.97$ )	2.99
f ( $\delta = 2.47 - 2.75$ )	3.04
g ( $\delta = 4.18 - 4.52$ )	3.13
h ( $\delta = 3.60 - 3.91$ )	3.07
j ( $\delta = 3.91 - 4.18$ )	1.03
k ( $\delta = 3.33 - 3.60$ )	1.01

**Table 3.1:** Normalized integrations for Figure 3.7 polymer peaks c-k. All peaks are normalized to the integration of peak c.

Figure 3.7 shows a characteristic  $^1\text{H}$  NMR spectrum for the synthesized polymer, along with its two constituent monomers; peaks are labeled such that they can be traced from the monomer to the polymer. First and most notable is the absence of peaks a and b on the polymer spectrum; this makes sense, as these two peaks correspond to the two protons on the methacrylate double bond, which see a drastic change in their electron environment during radical polymerization, changing to members of a carbon-carbon polymer backbone. Consequently, we do not expect to see these peaks in a sufficiently purified polymer, as their presence would indicate unreacted monomer. Instead, those proton signals shift significantly upfield to  $\delta = 2$ , where alkyl protons typically reside.<sup>[47]</sup> We additionally notice that peaks g-k all appear to shift downfield (most notably j). As the electron density of the a and b protons increases due to formation of a single bond from a double, we can infer that the alkyl protons near the methacrylate ester became relatively more electron poor, hence the downshifting.

Examining the integrations, we see that peaks c, j, and k, which all correspond to a pair of electrons on an alkyl carbon on ONBAMA, integrate to approximately unity. This indicates that all protons within these particular electron environments are incorporated onto the polymer chain, since peaks a and b are absent. Furthermore, we can confidently assume that the carbamate associated with the protected amine has not decomposed during the polymerization, since peak c integrates to the same

value as peaks j and k. The same can be said about peaks d-h for GMA; because they all integrate to  $\sim 3.0$  and additionally all correspond to a single electron, we can infer that GMA has incorporated stoichiometrically into the polymer and no undesirable side reactions have caused epoxide opening. To verify that the polymerization reaction has occurred stoichiometrically since we have confirmed no unreacted monomer exists, we can establish a system of equations where  $x_O$  corresponds to ONBAMA fraction in the polymer,  $x_G$  corresponds to GMA fraction in the polymer,  $n_x$  corresponds to the number of protons a peak  $x$  represents, and  $I_x$  corresponds to a particular peak  $x$ 's integration.

$$\frac{x_G}{x_O} = \frac{I_d/n_d}{I_c/n_c} = \frac{n_c I_d}{n_d I_c} \quad (3.1)$$

$$x_G + x_O = 1 \quad (3.2)$$

From this, utilizing the normalized integrations from Table 3.1 and the assignments from Figure 3.7, we find that  $x_G = 0.857$  and  $x_O = 0.143$ , which closely matches the monomer stoichiometry from the synthesis reactions (85:15). Utilizing any pair of peaks, so long as one is from ONBAMA and the other is from GMA, will yield a similar result due to the stoichiometry of both the integrations and the polymer composition. We can therefore confidently confirm the substitution of ONBAMA into the GMA polymer to be  $\sim 15\%$ , as designed.

### ***3.6 Processing Optimization & Performance***

#### ***3.6.1 Photoresist Processing***

*Substrate Preparation & Spin Coating:* Two considerations were necessary for adapting the protocols established in Chapter 2 to the PGMA-based photoresist. First, because we wanted to ultimately produce structures with through pores, an adhesion layer could not be deposited prior to the main structural resist. Though thin, the adhesion layer covers the entire substrate and, upon delamination, would lead to

pores that are occluded. Even if the bottom surface were to be cleaned or etched via a technique like O<sub>2</sub> plasma, the debris would likely contribute to pore occlusion. Second, because the desired application for the produced material is a water filter, or more specifically a pressure load bearing structure, we wanted to ensure that the photoresist film was as thick as possible, given the viscosity of the photoresist. Therefore, we elected to experimentally determine the slowest spin speed possible that would still uniformly coat the substrate: this was found to be 500 rpm. Faster resulted in appreciably thinner films, while slower often resulted in incomplete or visibly non-uniform substrate coverage. While there exist techniques to spin thicker layers with low-viscosity photoresists by spinning, baking, and spinning on top of the baked layer repeatedly,<sup>[68-69]</sup> we believed that this would introduce and magnify potential surface inhomogeneities that would naturally develop with additional substrate handling time, as well due to airborne particulates. Because we are utilizing a lithography technique that relies on direct photomask contact to the resist, we prioritized resist surface homogeneity when considering processing optimizations.

*Pre-Exposure Soft Bake:* The primary purpose of the pre-exposure soft bake (PSB) is to remove solvent from the resist film to limit the diffusion of polymer chains and photoacid molecules during and after exposure. Secondly, the PSB also can homogenize the photoresist surface due to resist reflow if it is heated sufficiently past the glass transition temperature of the resist. To optimize the PSB, there are two variables that can be controlled: temperature and duration. To determine the optimal temperature, we measured the mass of representative photoresist films as they were subjected to a stepwise temperature ramp from 30–100 °C, measuring every 2–5 minutes, with the temperature setpoint increased by 10 °C every 20 minutes. The recorded temperature of the hotplate was measured with an IR thermometer. This experiment is summarized by Figure 3.8. We observed that the masses of the films exhibit exponential decay-like trend when heated, with the greatest mass change occurring in the first 10-20 minutes of the experiment. We additionally note that each temperature increase appears to initiate the tail end of a new exponential decay event;

this makes sense: as the solvent content drops, liberating additional solvent at the same temperature becomes more difficult; but by increasing the temperature, the driving force for diffusion and evaporation increases along with the vapor pressure of the solvent remaining in the resist film. This behavior is most notable at 40 min during the transition from 40 to 50 °C. We additionally noted from this experiment is that solvent content appears to stabilize past 70 °C, such that additional temperature increase has no perceivable effect on sample mass. It is important to note that in the time between spin coating and the initial mass measurement, solvent likely evaporates from the resist film, so the idealized 100% mass at time 0 is dubious, which suggests that the curves might be stabilizing closer to 45% (the theoretical limit where a 45% solids resist can no longer lose mass from heating). This could indicate that at 100 min, when the temperature increases from 70 to 80 °C, we see negligible mass change because there simply is no solvent left to evaporate. Given that long PSBs at low temperatures are reported to have similar effect to shorter bakes at higher temperatures,<sup>[70-71]</sup> this required further examination. Further similar experimentation was performed to determine ideal duration, and ultimately a 10 min PSB was identified as ideal.

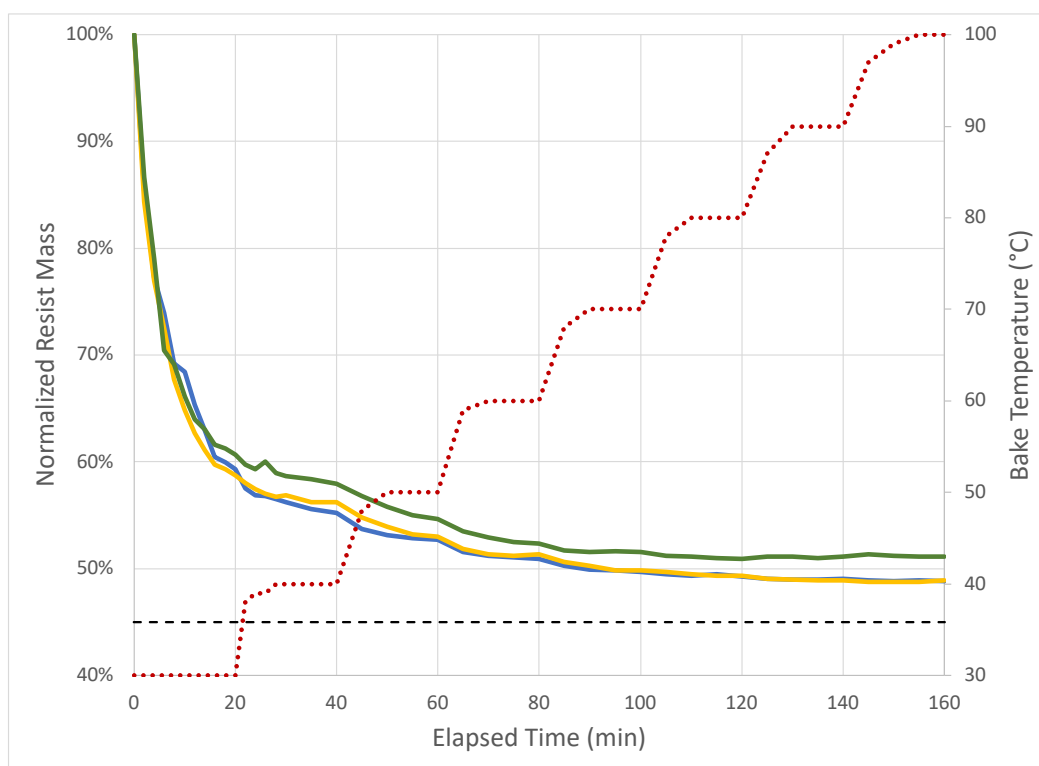


**Figure 3.8:** Solvent content of soft-baked films with temperature ramp. The masses of representative photoresist films were measured as they underwent a stepwise linear increase of baking temperatures. The dotted line represents the temperature of the hotplate when measurements were taken, and the dashed line indicates where no solvent would be remaining in a 45% solids photoresist.

*Exposure Dose:* Due to the method of exposure, the total applied optical dose is a spatiotemporal integral of the raster scanned Gaussian beam; the effective means for controlling that dose are variation of the nominal beam intensity (W) and the raster scan speed (mm/s). Initially, laser scan speed was believed simply to be a processing time optimization and was ignored, however this assumption introduced considerable challenge in identifying the proper optical dose. With a scan speed of 1.5 mm/s (per SU-8 processing conditions from Chapter 2), broad dose calibration tests were performed with a simplified Cr-on-glass photomask (see Section 4.2 for details), with targeted geometry as an array of 25  $\mu\text{m}$  circles spaced 12.5  $\mu\text{m}$  apart, such that the circles were void and the surrounding network were cross-linked polymer. the optimal PSB was used, while a second bake of 10 mins at 75  $^{\circ}\text{C}$  was selected as a

temporary post-exposure bake stand-in until it could be further optimized. Nominal selected doses were chosen ranging from 0.5-3.0 W. Representative samples from these experiments can be seen in Figure 3.10.

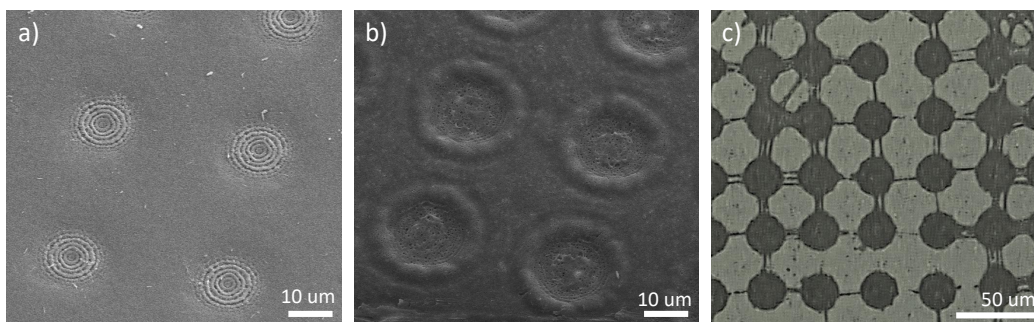


**Figure 3.9:** Micrographs of initial dosing experiments exhibiting heat damage. Nominal exposure doses are a) 2.0 W b) 1.4 W c) 1.0 W. Subfigures a & b are taken via SEM, while subfigure c was taken via optical microscope to maximize apparent contrast between substrate and cross-linked polymer.

For doses of and exceeding 1.4 W, our observations were simply that the entire photoresist layer was polymerizing despite the 25  $\mu\text{m}$  circular features on the mask obstructing incident light. While the presence of the Cr circular features is evident in 3.10a-b, the photoresist, if behaving optimally, should not polymerize beneath the mask features. While the source of this polymerization appears ambiguous from 3.10a-b, 3.10c demonstrates an unintuitive but telling phenomenon: the photoresist appeared to be curing as a positive resist rather than as a negative resist. More specifically, the circular features themselves were polymerizing, while the surrounding network was not; the exact opposite of what was intended. This clearly indicated the source of the unusual patterns in higher dose samples: heat damage. We were able to conclude that for high laser power  $\geq 1.0$  W, the delivered dose was being absorbed by the Cr features, elevating local temperatures, and inducing thermal cross-linking or polymer degradation. We believe this hypothesis to be a reasonable explanation, given that thermal cross-linking is expected in epoxide-based photoresist systems past 150  $^{\circ}\text{C}$ .<sup>[72]</sup> Because 1.0 W was not sufficient to polymerize the resist via optical dose, we elected to reduce the raster scan speed to allow for higher integrated optical dose but over a longer timeframe. By reducing the scan

speed to 0.5 mm/s, we expected we could reduce optical doses by a factor of 3 to deposit the same total optical dose while reducing the thermal load by allowing more time for heat to dissipate between line scans. To experimentally verify this assumption, we elected to characterize photoresist contrast, as shown below in Figure 3.10.

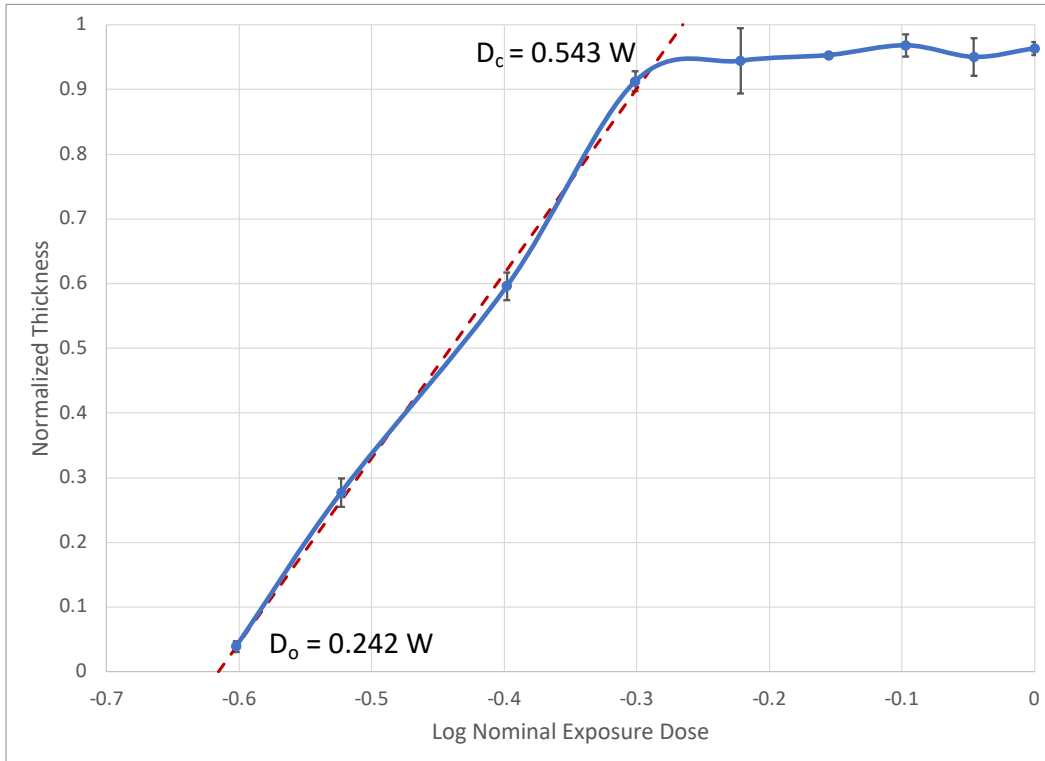


**Figure 3.10:** Optical dose contrast curve. Photoresist film thickness after exposure and development is examined as a function of optical exposure dose. The initial observable polymerization dose ( $D_o$ ) and the critical dose ( $D_c$ ) are extrapolated from a linear fit to the region prior to full thickness resolution.

$$\gamma = \left| \log_{10} \left( \frac{D_c}{D_o} \right) \right|^{-1} \quad (3.3)$$

Utilizing the Hurter-Driffield model<sup>[73]</sup> (Equation 3.3), we examined how photoresist thickness varies as a function of nominally applied optical dose. Samples were baked and exposed as before, but at a slower scan rate, and after development the film thickness was characterized via SEM. From the extrapolated doses, we determined

the first observable polymerization dose ( $D_o$ ) to be 0.242 W, while the critical dose ( $D_c$ ) was found to be 0.543 W. These bounds, when applied to the model, yield a contrast ( $\gamma$ ) of 2.85, which is within the bounds of expected values of other epoxide-based photoresist systems (1.0-3.0), and is a value comparable to that of SU-8.<sup>[74-76]</sup> Consequently, the optimal exposure parameters were selected to be 0.55 W scanned at 0.5 mm/s.

*Post-Exposure Bake:* The purpose of the post-exposure bake (PEB) is to increase the temperature and therefore diffusivity of photoacid and propagating polymer chains such that cationic polymerization occurs exclusively in exposed regions. As with the PSB, the PEB is controlled via two variables: temperature and duration. For photoacid-catalyzed polymer-based photoresists, the glass transition temperature ( $T_g$ ) is typically the lower limit for this bake, as for sufficiently high  $T_g$  diffusion is severely limited at operating/room temperature. Higher un-crosslinked  $T_g$  tends to be desirable when designing a photoresist system because it indicates strong intermolecular forces, such as through hydrogen bonding or dipole interactions, which further reduces diffusivity of propagating chains and generated photoacid. To identify the  $T_g$ , we utilized constant rate temperature ramping differential scanning calorimetry, as shown in Figure 3.12.

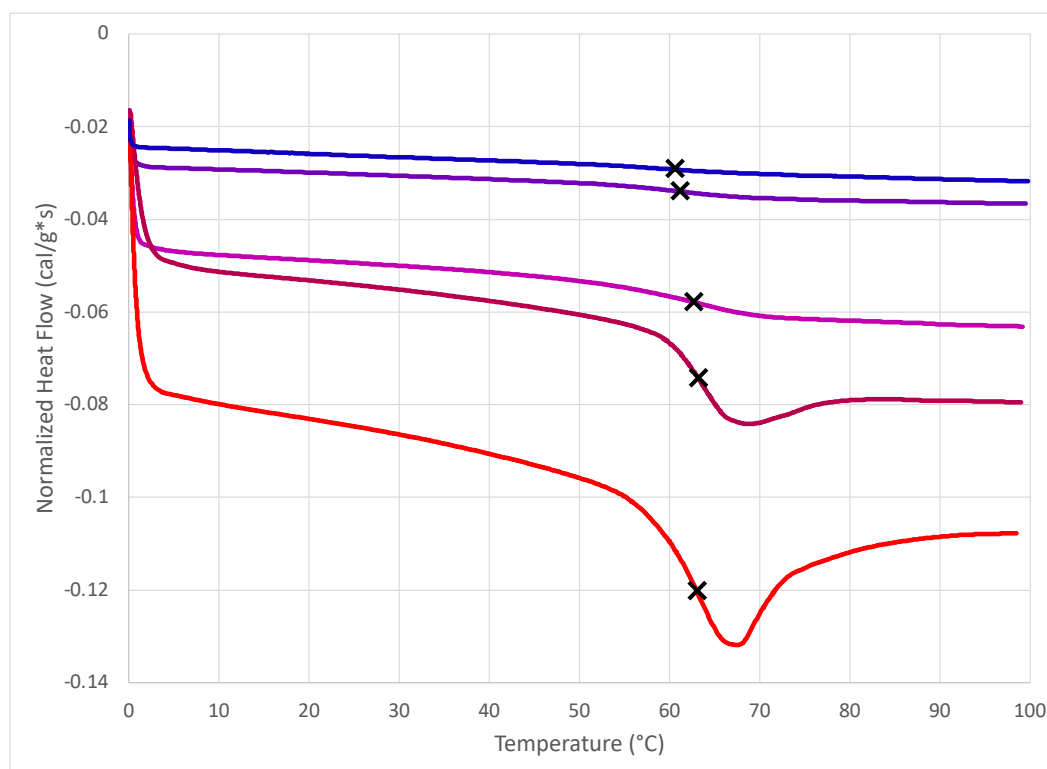


**Figure 3.11:** Differential scanning calorimetry of PGRO. Multiple ramp rates were used; from top to bottom, the ramp rates were 1.0 °C/min, 2.0 °C/min, 5.0 °C/min, 7.0 °C/min, and 10.0 °C/min.

Unlike first-order phase transitions such as melting, evaporation, and crystallization, which are identified by a discontinuous change in the first derivative of thermodynamic state variables or specific volume, the glass transition is identified as a second-order phase transition. This means that it exhibits continuity in the first derivative but a discontinuity in the second, or rather an abrupt, discontinuous change in a derivative property such as heat capacity. Consequently, by measuring heat flow into a sample undergoing a constant temperature ramp, changes in heat capacity can be observed by examining first and second derivatives of the normalized heat flow with respect to temperature.<sup>[77]</sup> To identify this point, we utilized the standard inflection point analysis technique, identifying the  $T_g$  for each temperature ramp as the point of most aggressive slope within the glass transition region, as indicated by selected points on each curve.<sup>[78]</sup> While we do observe a small dependence of the identified  $T_g$  with respect to ramp rate, the presence of a valley associated with

enthalpic recovery within the more aggressive ramp traces likely shifts the apparent  $T_g$  higher for those rates. Consequently, we identified the  $T_g$  of our 30 kDa PGRO product to be  $\sim 62$  °C, and therefore elected to set our PEB temperature above that, at 75 °C. While initial experiments were performed at lower temperatures, appreciable polymerization was not observed until a PEB temperature of 75 °C was selected. This is likely because molecular weight of propagating chains increases by  $\sim 30$  kDa per propagation event, severely limiting active site diffusivity. For a smaller molecule resist, such as SU-8, a PEB closer to the  $T_g$  is more appropriate, as the diffusivity likely is less dependent on single cross-linking events, but for sufficiently large molecules, further increasing the PEB temperature past the  $T_g$  is necessary to facilitate multiple cross-linking events per active site. To determine duration, samples were simply baked at a range of available times, and the best macroscopic feature resolution was selected (such as border and mask label), which was exhibited at 20 min (Figure 3.13).

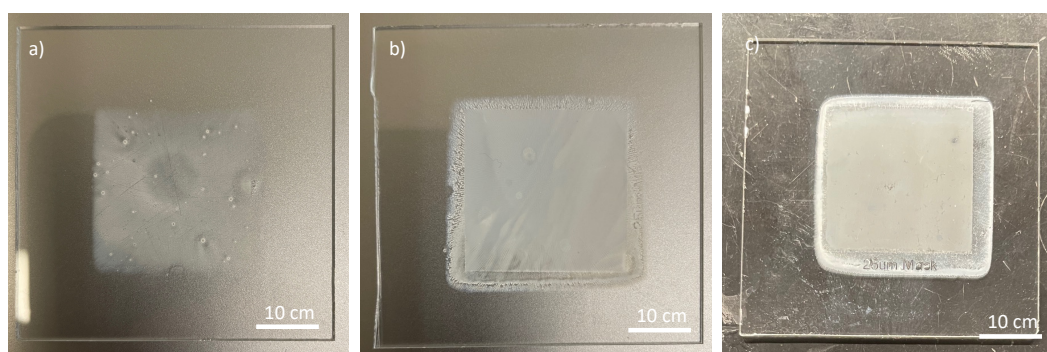


**Figure 3.12:** Varied PEB durations. 30x30 mm samples exposed with optimized conditions were subjected to a) 5 min, b) 10 min, and c) 20 min PEB. Resolution of edges and coloration homogeneity were indicating factors when selecting optimal duration.

### 3.6.2 Lithographic Performance

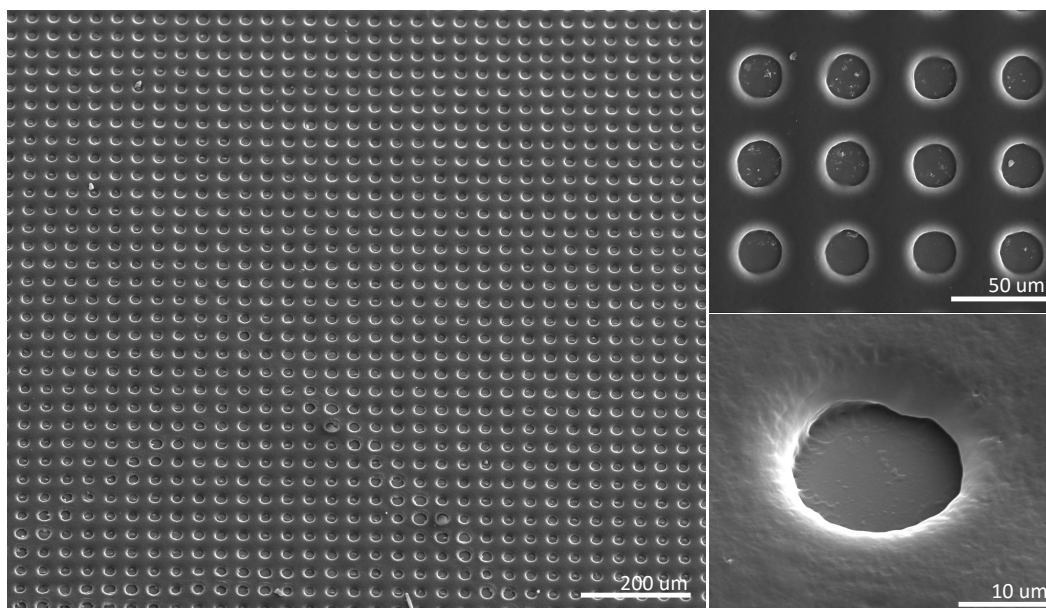


**Figure 3.13:** 25 um pore matrix resolved in PGRO photoresist. 30x30 mm samples exposed with optimized conditions were examined under SEM at a variety of different magnifications.

Utilizing the optimized exposure conditions, we successfully demonstrated the resolution of our targeted structure: a periodic square array of 25 um pores, as exhibited in Figure 3.14. Surface and pore uniformity is excellent, with slight variations in pore geometry caused only by scratches on photoresist films. A series of 100 pores were randomly selected from a series of top-down SEM micrographs and the resultant diameter was found to be only  $20.43 \pm 1.38$  um. Magnified examination of individual pores shows poor anisotropic wall resolution, featuring a surrounding region of sloped photoresist with increasing thickness. 30 of these sloped surrounding regions were characterized in a similar fashion, indicating that they add  $2.78 \pm 0.36$  um to the apparent patterned region, yielding a final average pore diameter of  $23.21 \pm 1.47$  um with standard deviation error propagation.

The discrepancy between targeted and resolved pore diameter indicates that resolution has not been maximized; literature indicates that submicron features are well within the expected resolution limit of a visible light sensitive GMA-based

photoresist,<sup>[47-50]</sup> which further suggests that truly optimal lithographic parameters were not identified. The sloped region surrounding the pore is potentially the result of photoacid diffusion from an excessively long PEB; as photoacid diffuses, the diffusion gradient that would result could produce a reasonably linear concentration profile of photoacid and active polymerization sites, resulting in thinner residual material post-development, per Figure 3.11. This thinner material could reasonably manifest as this apparent sloped ring reaching out to a more reasonable feature diameter.

Another potential explanation for this discrepancy is the incomplete elimination of thermal cross-linking effects from the exposure procedure. While the instantaneous thermal load was dropped by lowering scan and exposure power, it is possible that heat dissipation still was not sufficient to keep the Cr absorbing features at reasonable operating temperatures. Even light thermal cross-linking could lead to residual material clinging to the sidewalls during development, forming a similar sloped morphology. We did not quantify the thermal load of the laser in this study; however further examination may be necessary to appropriately diagnose feature resolution issues. We believe this to be a critical finding of this study; namely that for sufficiently large photoresist molecules with considerably lower diffusivity than SU-8, thermal load of the laser has a clear and marked effect on pattern resolution and feature morphology, and this phenomenon would benefit from additional examination.

Lastly, we believe there could be an additional effect from unoptimized photoresist development. A duration of 20 min was initially selected as a baseline for comparison, and ultimately pattern resolution was sufficient such that other conditions took precedence during optimization and iteration. It is possible that a longer development time would more appropriately resolve the pores to expected size; the caveat to this claim, however, is that for durations exceeding 20 min, sample delamination from the substrate was typically observed, resulting in an unsalvageable

film. As the polymer network becomes swollen with developing solvent, it loses structural integrity, and upon delamination from the substrate, the film tended to clump and tangle upon itself, rendering it unusable as a thin membrane filter. SU-8 and other epoxide photoresists are known to have poor adhesion to glass substrates, so delamination is a reasonable expectation; and given that samples require post-development delamination to function as a proper filtering membrane, increasing adhesion was deemed disadvantageous considering the design goals of this work. We therefore conclude that the poor feature size resolution is likely a combination of these factors with varying significance, and that further campaigns of optimization and iteration would be required to more ideally resolve features and anisotropic walls properly.

### ***3.7 Experimental Methods***

*ONBAMA Synthesis:* To a 100 mL round bottom flask were added 10.0 g (65.3 mmol) *o*-nitrobenzyl alcohol (97%, Sigma Aldrich), 9.7 mL (68.6 mmol) 2-isocyanatoethyl methacrylate (98%, TCI Chemicals), and 20 mL toluene (ACS reagent, Sigma Aldrich) as a solvent. Vessel was placed in a mineral oil bath at room temperature, attached to a water-cooled reflux column, and deoxygenated via dry N<sub>2</sub> sparging for 15 minutes. Bath was heated to 115 °C and left to react for 2 h, then allowed to cool back to room temperature. Reaction mixture was mixed with excess hexanes (OmniSolv, Sigma Aldrich) in liquid-liquid extraction funnel 3 times, and resulting brown viscous liquid was isolated from hexanes phase. Viscous liquid was collected in a sample jar and vacuum dried until a dry, off-white or khaki crystalline solid remained.

*Pre-Polymerization, FRP:* To a 500 mL round bottom flask were added 28.0 mL (0.211 mol) glycidyl methacrylate (97%, Sigma Aldrich), 11.48 g (38.2 mmol) ONBAMA, and 1.63 g (9.92 mmol) azobisisobutyronitrile (98%, Sigma Aldrich) initiator alongside 250 mL tetrahydrofuran (ACS reagent, Sigma Aldrich) as a

solvent. Vessel was attached to a water-cooled reflux column and deoxygenated via dry N<sub>2</sub> sparging for 45 minutes. Vessel was lowered into a pre-heated oil bath at 70 °C and allowed to react for 5 h, after which the vessel was removed from the oil bath and reoxygenated to terminate radical reaction. Reaction mixture was then vacuum filtered through Celite S (Sigma Aldrich) and rotovapped to a low-volatility viscous liquid. ~25 mL tetrahydrofuran was added to redissolve polymer and polymer was precipitated via drop-wise addition to large excess of diethyl ether (ACS reagent, Sigma Aldrich). White solid was vacuum filtered and subsequently vacuum dried until a dry, white solid remained.

*Pre-Polymerization, ATRP:* Prior to reaction, glycidyl methacrylate (97%, Sigma Aldrich) was passed through a basic alumina column to remove trace inhibitors. Separately, a catalyst stock was prepared of 32.5 mg (0.146 mmol) copper (II) bromide (>98%, TCI Chemicals) and 42.0 mg (0.145 mmol) tris(2-pyridylmethyl) amine (98%, TCI Chemicals) dissolved in 10 mL dimethyl formamide (ACS reagent, Sigma Aldrich). Separately, an initiator stock was prepared of 93.0 mg (0.566 mmol) azobisisobutyronitrile (98%, Sigma Aldrich) dissolved in 15 mL dimethyl formamide. To a 100 mL round bottom flask were added 10.5 g (34.0 mmol) ONBAMA, 25.5 mL (192 mmol) filtered glycidyl methacrylate, and 40 mL anisole (Sigma Aldrich) as a solvent. To the reaction vessel were additionally added 2 mL catalyst stock and 3 mL initiator stock. The reaction vessel was then deoxygenated via N<sub>2</sub> sparging for 30 minutes, after which 573  $\mu$ L (3.0 mmol) diethyl 2-bromo-2-methylmalonate (98%, Sigma Aldrich) ATRP initiator was added while maintaining inert atmosphere. The vessel was lowered into a pre-heated mineral oil bath at 60 °C and left to react for 8 h, after which the vessel was removed from the bath and reoxygenated to terminate radical reaction. Reaction mixture was then vacuum filtered through first Celite S (Sigma Aldrich) and subsequently through basic alumina to remove Cu catalyst complex. rotovapped to a low-volatility viscous liquid. ~25 mL tetrahydrofuran was added to redissolve polymer and polymer was precipitated via drop-wise addition to large excess of diethyl ether (ACS reagent,

Sigma Aldrich). White solid was vacuum filtered and subsequently vacuum dried until a dry, white-to-mint green solid remained. Green coloration was indicative of trace  $\text{Cu}^{2+}$  contamination.

*Photoresist Preparation:* To an amber glass scintillation vial were added 400 mg HNu 254 (Spectra Group Ltd), 40 mg HNu 470 (Spectra Group Ltd), and 40 mg cationic accelerator (Spectra Group Ltd), along with 10.29 mL cyclopentanone (ReagentPlus, Sigma Aldrich). The solution was heated and stirred at 75 °C until all solids dissolved. To the initiator solution was added 7.52 g synthesized PGRO. The vial was then placed in a vortex shaker and allowed to mix overnight or until a homogeneous optically clear polymer solution resulted. The crude photoresist solution was then filtered through 0.45  $\mu\text{m}$  PTFE syringe filters (VWR) into a new vial and allowed to rest capped until no bubbles were visible in photoresist. The photoresist solution was stored in an inert atmosphere when not in use.

*Lithographic Sample Preparation:* A 1 mm thick 2x2 inch soda lime glass slide (VWR) was cleaned and sprayed first with acetone, then with isopropanol (Sigma Aldrich) and dried with a  $\text{N}_2$  gun. Photoresist was spin coated at 500 rpm for 30 seconds, after which edge beads were removed via razor blade and the sample was baked on a hotplate at 75 °C for 10 min to remove solvent. The resulting 5–10  $\mu\text{m}$  photoresist film and substrate were allowed to cool and were then mounted onto the black lithography stage with 4 drops of mineral oil (VWR) to facilitate contact with the stage and to avoid interfaces due to air gaps. 4 drops of mineral oil were placed directly onto the photoresist, where the photomask (Digidat) was then placed feature-side down, and gentle pressure was applied to facilitate ideal contact. Photoresist was then exposed via technique outlined in Chapter 2, with laser power 0.55 W, scan speed 0.5 mm/s, and raster offset 0.4 mm. After exposure, sample was removed from the lithography stage and mineral oil was gently wiped off with TexWipes. The sample was then baked on a hotplate at 75 °C for 20 mins, subsequently removed from the hotplate, and allowed to cool to room temperature. Photoresist was

subsequently developed in propylene glycol monomethyl ether acetate (Fisher Scientific) for 20 mins, after which the sample is placed in isopropanol for 20 mins to de-swell the polymer and remove residual developer solution. Finally, the sample is removed from the isopropanol and allowed to air dry at room temperature.

*<sup>1</sup>H NMR Spectroscopy:* 20 mg or 20 uL (depending on phase) sample were dissolved in 600 uL deuterated chloroform (Sigma Aldrich) and pipetted into an 8" NMR tube (VWR). Spectra were taken on a Varian 500 MHz spectrometer with CDCl<sub>3</sub> reference ( $\delta = 7.26$ ). Spectra were baseline corrected, phase corrected, and quantified via the MestReNova software package.

*Gel Permeation Chromatography:* Performed using an Agilent 1260 pump connected to two PLgel mixed-B 10 um columns. Signals were detected via an Agilent 1200 series diode array detector, a Wyatt 18-angle DAWN HELEOS light scattering detector, and an Optilab rEX differential refractive index detector. The mobile phase was tetrahydrofuran at a flow rate of 1 mL/min. Molecular weight data were calculated via light scattering using a measured dn/dc of 0.087.

*Optical Microscopy:* Optical microscope images were taken on an Olympus BX51M in bright field mode with 5x, 10x, and 50x objective lenses.

*Scanning Electron Microscopy:* Performed in either a FEI Versa 3D DualBeam or a FEI Quanta 200 at 5-20 kV. A 5 nm platinum coating was sputtered onto samples prior to imaging to reduce sample damage and charging.

*Differential Scanning Calorimetry:* Performed on a TA Instruments DSC250 on the temperature range 0-100 °C at ramp rates 0.50, 1.0 2.0, 5.0, 7.0, and 10.0 °C/min for powdered unexposed photoresist polymer samples.

### ***3.8 Summary & Outlook***

In this chapter, we demonstrated the design and synthesis of a GMA-based negative-tone photoresist with an incorporated photo-caged amine for future surface functionalization. NMR and GPC indicate that synthesis of sufficiently small oligomers for use in a photoresist was reproducible with both FRP and ICAR ATRP, and that random co-polymer stoichiometry matched that of initial monomer feedstocks. The incorporation of ONBAMA into a photoresist to serve as a facilitator of photo-patternable surface functionalization has not been demonstrated in literature and is an exciting new means for tailoring surface chemistry. We identified optimal PSB conditions by measuring time-resolved solvent content within films baked across a range of temperatures and confirmed reproducibility. We identified optimal laser exposure conditions by establishing a Hurter-Driffield contrast curve to quantify critical and clear doses, which resulted in a measured contrast of 2.85, which appropriately matches similar photoresist mechanisms and chemistries as reported in literature. PEB time and duration were optimized by examining the polymer  $T_g$  via DSC, providing a benchmark for identifying temperatures where diffusivity begins to noticeably increase. Lastly, we demonstrated that utilizing the identified processing conditions, an array of open circular pores can be resolved with error in feature size resolution of  $\sim 10\text{-}20\%$ . Despite the potential for future iterative improvement of these processing conditions, we deemed that produced materials would be sufficient for surface functionalization and preliminary filtering experiments, to be detailed in Chapter 4.

The chemical functionality that ONBAMA provides affords this photoresist a wide range of potential surface-mediated capabilities; for example, conjugation and capture of proteins for development of complex flow assays for biological testing, or affixation of light-responsive nanoparticles for inducing thermal material responses such as shape memory.<sup>[79-80]</sup> Additionally, because the carbamate photodegrades, produced films with this photoresist could be used as substrates for UV lithographic

surface functionalization, enabling surface chemistry hierarchy and selectively well beyond the capabilities of more traditional surface functionalization and treatment techniques.

*Chapter 4*

## WATER FILTER DESIGN &amp; CHARACTERIZATION

**4.1 Filter Design**

Samples manufactured from SU-8 and from PGRO photoresists were examined for water permeability utilizing the metasurface utilized in Chapter 2, however no reasonable head pressure applied saw initiation of fluid flux. Consequently, a new mask was necessary, as the geometry of the produced structure is directly tied to the mask's interference pattern. While our collaborators in the Faraon lab began to develop a new metasurface mask that can produce an interference pattern more amenable to open pore resolution, we elected to devise a simple substitute in the interim to provide proof-of-concept for application of the technique to water filtration devices. To that end, we designed a simple mask consisting of Cr circles on glass arranged in a square array pattern, such that upon pattern transfer via a negative-tone resist like SU-8 or PGRO, the surrounding matrix would resolve while leaving circular holes unpolymerized; the mask design and resulting structure can be examined in Figure 4.1.

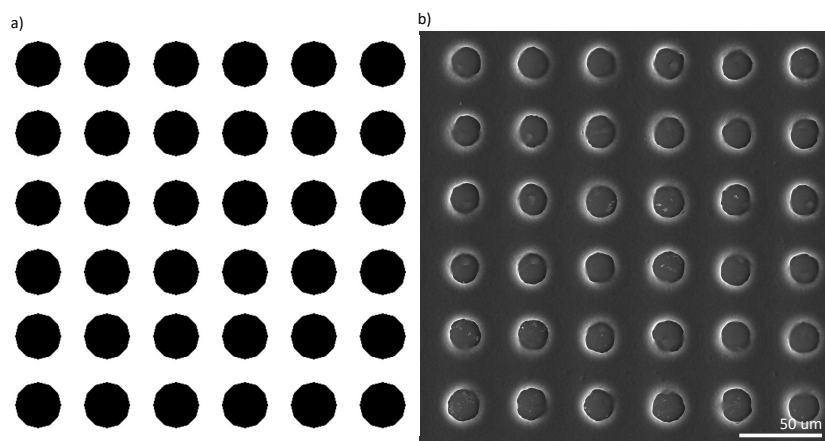


**Figure 4.1:** Filtration mask and resulting structure. a) Schematic drawing produced in *AutoCAD* to provide of simple Cr-on-glass mask. Circles representing Cr features are 25  $\mu\text{m}$  in diameter, with

center-to-center offset of 37.5  $\mu\text{m}$  to result in a 60% relative density structure negative. b) Material produced with designed mask, per protocols in Chapter 3 under identical conditions to samples presented in Figure 3.14.

This geometry was selected for a variety of reasons including ease of resolution and effectively guaranteed efficacy, but additionally it provided a simple geometry that could be explored both analytically and computationally. Regarding the former, we initially chose to employ the Lucas-Washburn equation (Eq. 4.1), as a means for understanding fluid penetration into circular pores.<sup>[81-82]</sup>

$$\frac{dh}{dt} = \frac{\left(P_A - \rho gh + \frac{2\gamma_s \cos\theta}{r}\right) (r^2 + 4\epsilon r)}{8\mu h} \quad (4.1)$$

$$h_{eq} = \frac{2\gamma_s \cos\theta}{\rho gr} \quad (4.2)$$

Here,  $h$  is capillary rise height,  $t$  is time,  $P_A$  is unbalanced atmospheric pressure,  $\rho$  is the imbibing fluid density,  $g$  is acceleration due to gravity,  $\gamma_s$  is force attributed to surface tension per area,  $\theta$  is the meniscus contact angle,  $r$  is the effective radius of the pore,  $\epsilon$  is the coefficient of slip, and  $\mu$  is the viscosity of the imbibing fluid. When simplified, noting that atmospheric pressure is balanced in an open system and therefore can be evaluated as zero, the expression collapses to the accepted Jurin equation for equilibrium height.<sup>[82]</sup> In our case, when evaluating for capillary rise in a single tube of diameter 25  $\mu\text{m}$ , we determine equilibrium capillary rise to be  $\sim 70$  cm. Experimental results suggest that this theoretical value is a considerable overestimation, and that the Lucas-Washburn equation is sufficient for explaining capillary rise only in roughly the first 10% of maximum capillary rise due to its negligence of gravity and inertial forces at large time scales.<sup>[83-84]</sup> With this in mind, we explored how a single pore might be imbibed with fluid after sufficient wetting has taken place via a 2-phase phase-field simulation performed in *COMSOL Multiphysics*, the results from which proved to be trivial. For all simulated pore diameters ranging from 5-50  $\mu\text{m}$ , pores were expected to fill completely within microseconds.

Macroscopically, further processing of the membranes produced in Chapter 3 was required to produce samples for water flow-through experiments. To delaminate the membranes, after development and air drying, samples were placed in a buffered hydrofluoric acid (HF) bath for ~3 h or until the membrane visibly detached from the substrate and floated to the surface. Membranes were then gently placed onto a 3D-printed square lattice capture mesh manufactured in PR48 resin with unit cell dimension 1 mm and beam diameter 250  $\mu\text{m}$  and rinsed in DI water to sufficiently remove etchant. After air drying, the membrane remained affixed to the capture lattice (Figure 4.2), which now provided considerable support to the fragile membrane, allowing for distribution of pressure loads during subsequent water permeability experiments.

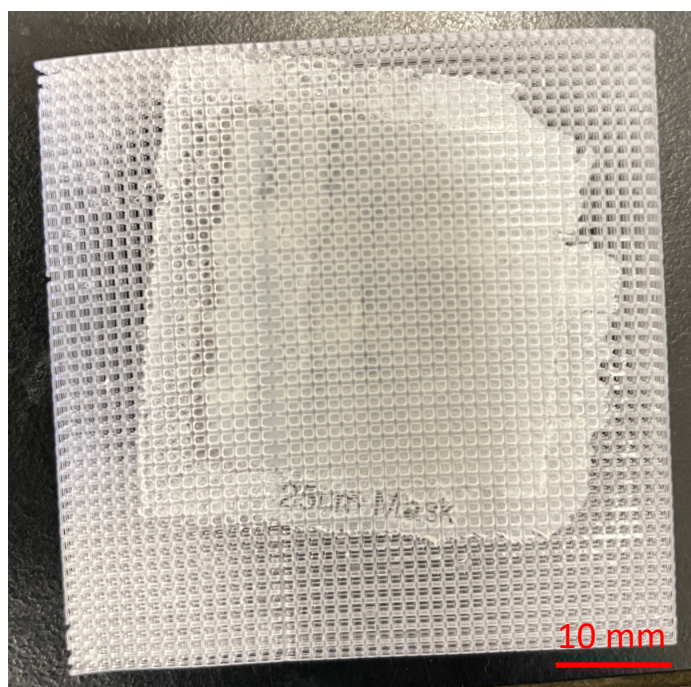


**Figure 4.2:** Delaminated filtration membrane. Capture lattices serve to support the incredibly fragile filtration membranes. Damage incurred during delamination is evident in the top right corner; surface tension induced cracks resulted in the loss of the monolithic region as the membrane floated to the surface of the etchant bath. The patterned/porous region can be observed as an opaquer square within the monolithic border region.

## 4.2 Hydrophilicity & Water Permeability

To explore produced membrane water permeability to address hydrophilicity and fluid transmission required by design goal #2 outlined in Chapter 3, we first examined water contact angle on a series of membranes produced in both SU-8 and PGRO photoresists. Representative images from these experiments are shown in Figure 4.3.

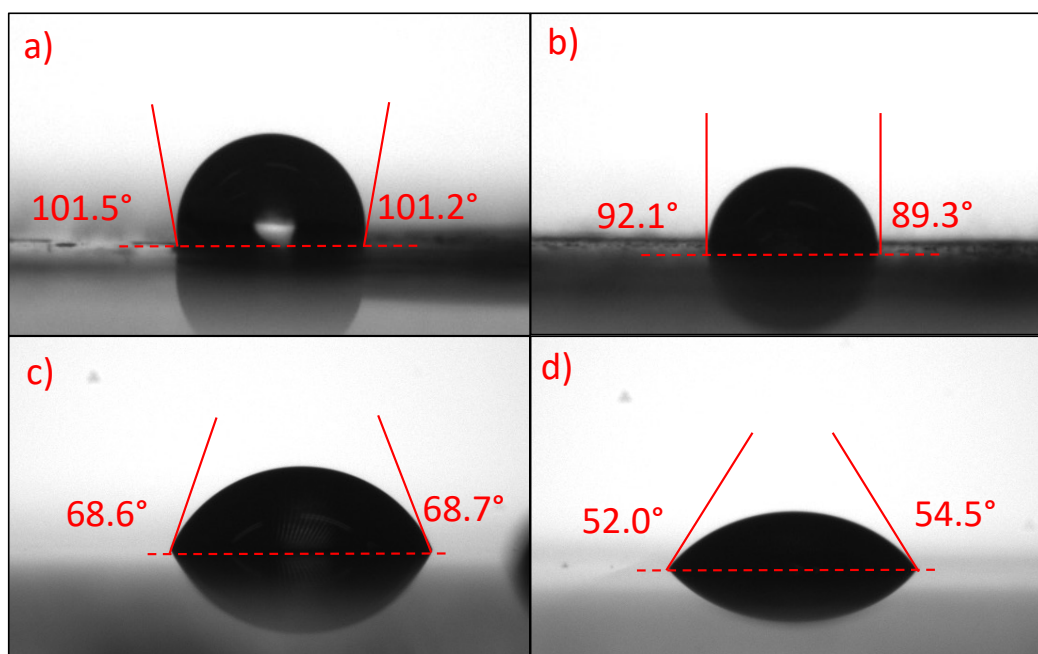


**Figure 4.3:** Water contact angle experiments. Water droplets were examined as they contacted both SU-8 (a & b) and PGRO (c & d) membranes. Shown are the maximum and minimum observed contact angles.

We observed a wide range of contact angles on a series of different films and sample regions. We attribute this wide range to considerable variation in surface roughness from sample to sample. For hydrophilic materials, surface roughness is expected to decrease contact angle (and therefore increase relative hydrophilicity) due in large part to increased surface area.<sup>[85]</sup> Irrespective of the range, it is abundantly clear that PGRO films are considerably more hydrophilic than SU-8 films. We attribute this to the greater number of groups available for H-bonding present on the ONBAMA monomer compared to the GMA monomer naturally increasing hydrophilicity.

Membranes submerged in water and subsequently surface dried were then subjected to preliminary water passthrough experiments by placing DI water droplets dyed with methylene blue directly onto vertically oriented membranes. The resulting transient behavior was captured on video and analyzed in ImageJ and VLC to determine time-resolved surface area approximations. Due to the support structure, volume and mass retention experiments within the membrane specifically were not accessible via this technique. The results of this experiment are shown in Figure 4.4.

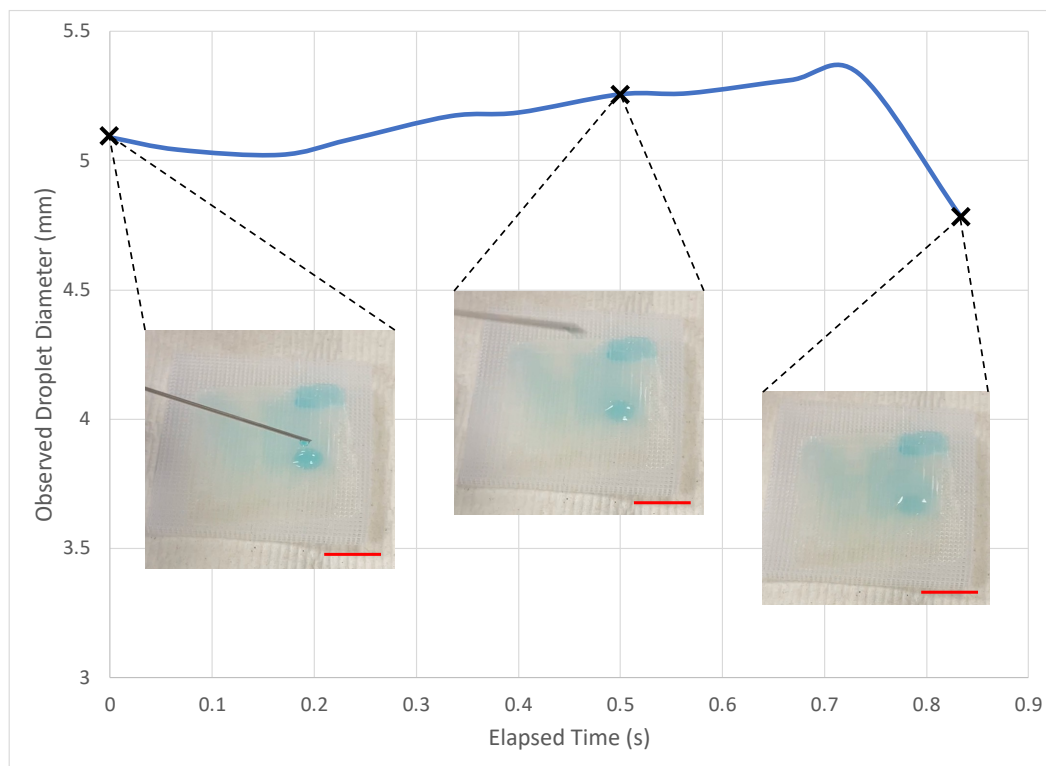


**Figure 4.4:** Droplet diameter vs time. Droplet diameter was tracked via ImageJ according to values of blue color intensity, with manual adjustments as necessary. Stills from a representative video are shown at  $t=0$ ,  $t=0.5$ , and  $t=0.83$  s. Scale bar for each inset is 10 mm.

After an initial small decrease in size, droplet diameter appeared to grow steadily during its  $\sim 1$  s lifetime. This suggests that flux occurred non-uniformly throughout the droplet, and likely greater mass transfer occurred towards the center of the droplet due to its greater height compared to the edges. This is further suggested by the apparent motion of light patterns on the surface of the droplet, as it appears to flatten

out as the video progresses. This is consistent with literature examination of similar phenomena, namely that fluid horizontally spreads across the surface as it imbibes vertically into the porous medium.<sup>[86-87]</sup> Because droplet heights were not measurable directly in this experiment, localized flux was not calculable, however bulk transport properties can be approximated. From the video, we observed that the nominal 50  $\mu\text{L}$  droplet existed on the membrane for 27 frames of a 30-fps video, indicating a total mass transfer time of 0.90 s. Evaluating the contact area between the maximum and minimum droplet diameters yield a contact area of 20.3 – 22.4  $\text{mm}^2$ , indicating an average volumetric flux of 2.61  $\pm$  0.36  $\mu\text{L mm}^{-2} \text{s}^{-1}$ . While further quantification can be done to better understand the fluid mechanics associated with the fabricated membranes, this series of experiments serves as a proof-of-concept and verification that materials manufactured with PGRO have potential to serve as water permeable membranes, sufficiently satisfying design requirement #2.

#### ***4.3 Deprotection Verification & Surface Characterization***

To evaluate design goal #3 and determine the functionalization potential of PGRO photoresist, we first aimed to evaluate whether the deprotection can occur in solid phase. Per literature reports,<sup>[66]</sup> poly(ONBAMA) homopolymer amine deprotection reaches its peak efficiency between 16-24 h in solution under constant irradiation with a UV-C bulb. We aimed to replicate this experiment in solid phase, utilizing the color of the photoresist as an indicator of deprotection, since the *o*-nitrobenzyl containing aldehyde side product of the deprotection (Figure 3.4) is dark brown in coloration.

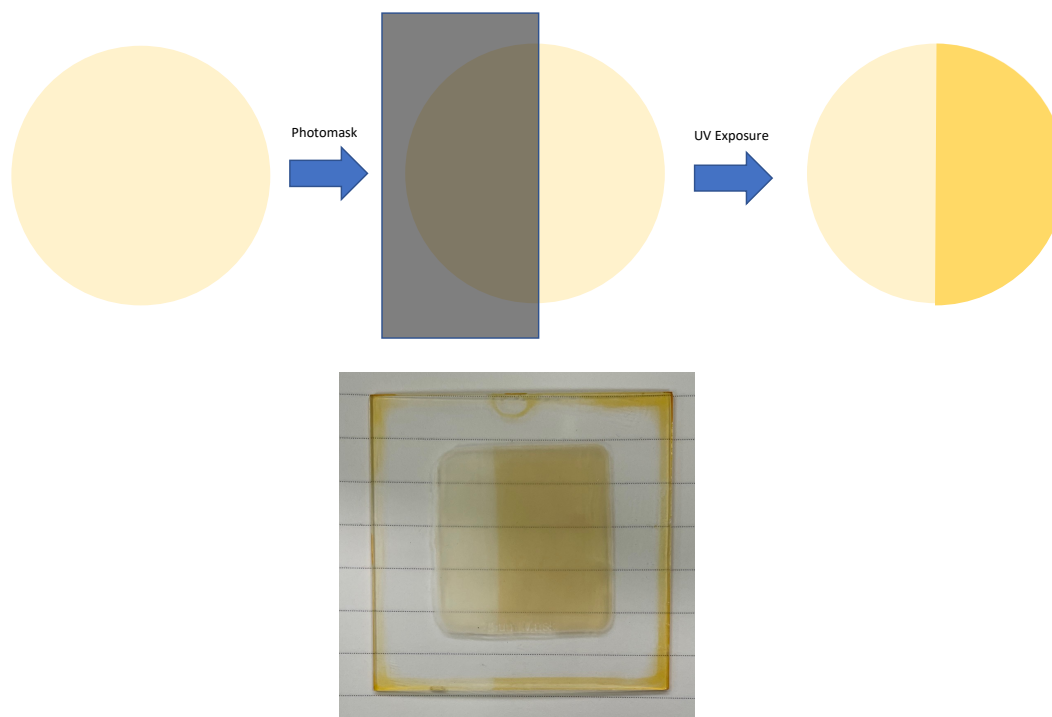


**Figure 4.5:** Solid phase PRGO deprotection. A schematic of the experiment shown above, with the result of the experiment shown below after 24 h UV-C exposure. Darker coloration is indicative of successful ONBAMA deprotection.

As seen in Figure 4.5, 24 h irradiation does successfully introduce the expected coloration change, indicating that deprotection of the amine did occur. Upon submersion in a swelling solvent, the darker color appeared to leech out into the solution, returning the polymer more closely to its original coloration, which is to be expected since the liberated aldehyde is no longer bound to the photoresist network. To examine the reactivity of the amines liberated by ONBAMA degradation, we placed similarly processed membranes into carbonate-buffered water baths and added a fluorescein isothiocyanate dye (FITC), which is traditionally used to label the N-terminus of proteins.<sup>[88-89]</sup> We expected for the liberated amines to react akin to the N-terminus of a protein with the thiocyanate on FITC to form a thiourea group, covalently attaching the fluorescent group to the polymer backbone. After overnight soak in the FITC bath, samples were washed with a FITC-free buffer and air dried. Samples were then examined under confocal microscopy in dark-field mode and irradiated with 490 nm; representative images are shown in Figure 4.6.

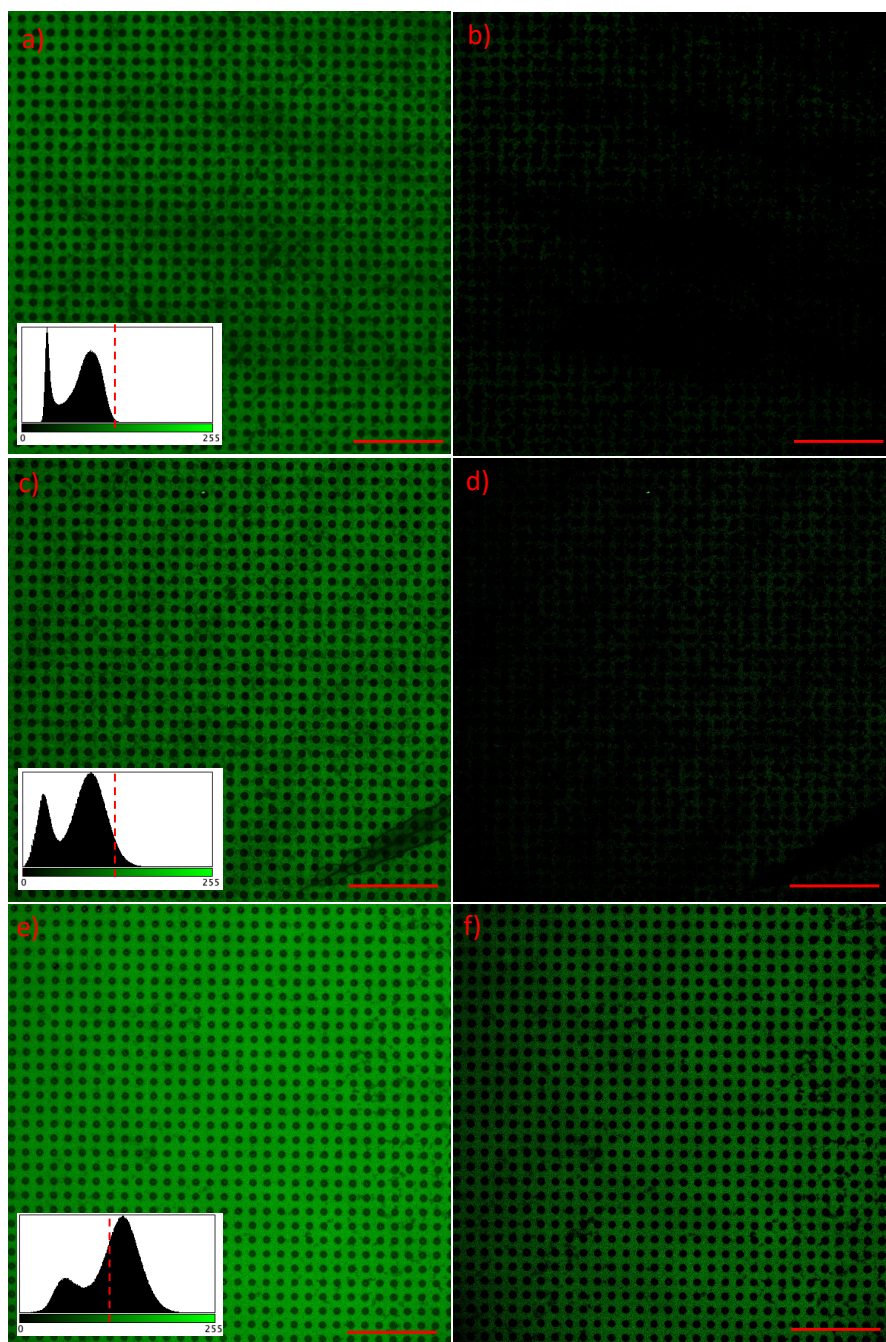


**Figure 4.6:** Confocal fluorimetry of FITC treated PRGO membranes. Subfigures a & b are representative micrographs of a membrane not treated with FITC and not exposed to UV before and after baseline correction, subfigures c & d are representative micrographs of a membrane treated with FITC that was not exposed to UV before and after baseline correction, and subfigures e & f are representative micrographs of a membrane treated with FITC that was exposed to UV before and after baseline correction. The left column corresponds to raw fluorescence signal, with inset histograms displaying binned raw intensity. Red dashed line corresponds to background correction threshold. Scale bars all correspond to 250  $\mu\text{m}$ . Figures are colorized to correspond to excitation/emission wavelengths.

As expected, whether from the polymer itself or the photoinitiating systems, considerable background autofluorescence was observed, and therefore baseline correction was necessary. To properly identify the baseline fluorescence signal, we imaged samples in three categories: a true control, a negative sample, and a positive sample. The true control was not treated with UV-C or FITC, while the negative sample was treated with FITC but was not exposed to UV-C. The positive sample was treated with both. From the appearance and intensity histograms, we observed that the control and negative samples exhibit similar fluorescence intensity and distribution, which suggests that without exposure, FITC cannot bind to the surface, as expected. With UV exposure, however, we saw that the signal distribution increases in intensity. By establishing a normalized baseline at 95/255, per the maximum intensity observed in the control sample, we adjusted the image brightness to eliminate the signal from background autofluorescence, resulting in the left column of Figure 4.6. Here, the stark difference between the unexposed and exposed samples becomes evident, indicating clearly that deprotection facilitated the covalent capture of the FITC dye. Unfortunately, this labelling technique does not provide a quantitative assessment of functionalization density, and therefore we cannot comment on the efficiency of the functionalization; however on a binary scale, it is clear that functionalization of the surface did in fact occur in desired (exposed) regions. Consequently, this series of experiments serves as a proof-of-concept and verification that materials manufactured with PGRO can be easily and selectively functionalized via post-processing treatment with UV-C and an electrophilic functionalizing agent, properly satisfying design goal #3.

#### ***4.4 Experimental Methods***

*Sample Delamination:* Samples produced via the lithography technique outlined in Chapter 3 were submerged in a shallow bath of buffered HF (provided by Kavli Nanosciences Institute) and allowed to rest for 3 h. After sufficient submersion, membranes were gently detached by running a flat plastic tweezer between the

membrane and the glass substrate, causing the membrane to float to the surface. A 3D printed capture lattice (PR-48, fabricated on an AutoDesk Ember) was submerged into the HF and gently tapped until all bubbles retained in the lattice appeared to exit the structure. The lattice was gently raised underneath the floating membrane until contact was made, and the lattice and membrane were transferred to a DI water bath to remove HF. After a 1 h soak, the capture process was repeated, and the samples were allowed to air dry.

*Contact Angle Measurements:* Contact angle was measured via the contact angle goniometer provided by the Molecular Materials Resource Center within the Beckman Institute. The instrument consists of a syringe mounted above an elevated stage which is imaged via a U4 Series SuperSpeed Ramé-Hart camera and analyzed using *Ramé-Hart DropImage*.

*Droplet Flux Measurements:* Membranes affixed to their capture membranes were submerged in DI water and allowed to soak until air bubbles no longer were retained in the structure, approximately 10 min. 0.5 mL methylene blue dye (Sigma Aldrich) was added to ~100 mL of water to serve as the transmitted fluid. Membranes were removed from their water bath and water was drained from the membrane via wicking from a KimWipe, and was allowed to dry for ~30 min. 50 uL droplets were pipetted directly onto the surface, and the resulting flow behavior was recorded by video on an Apple iPhone 12 12MP camera. Resulting videos were analyzed frame-by-frame in *VideoLAN VLC Media Player* and the frame still images were analyzed in *ImageJ*.

*FITC Labelling:* Still laminated samples produced via the lithography technique were submerged in dilute nitric acid (1.0 M, Sigma Aldrich) for 24 hr to sufficiently open remaining epoxides. Samples were removed and soaked in DI water to sufficiently remove acid and allowed to air dry. Samples were then wrapped partially in aluminum foil (serving as a photomask) and were placed under a 4 W Spectroline E-Series UV lamp operating at 254 nm for 24 h. A carbonate buffer was prepared in a

250 mL crystallization dish by mixing 100 mL DI water with the contents of a carbonate-bicarbonate buffer capsule (Sigma Aldrich), the exposed sample was placed in the buffer, and the dish was placed on an orbital shaker to provide gentle agitation. In 0.5 mL anhydrous DMSO (VWR) was dissolved 0.5 mg fluorescein isothiocyanate isomer I powder (Sigma Aldrich), and this solution was pipetted slowly into the buffer at 5 uL increments every 5 minutes until 35 uL had been added, at which point the dish was covered in aluminum foil was left undisturbed at room temperature for 18 h. Sample was removed from the FITC-containing buffer and placed into a fresh buffer solution and allowed to soak covered for an additional 6 h, after which it was rinsed with DI water and allowed to air dry while remaining covered. Samples were promptly imaged to avoid photobleaching.

*Confocal Microscopy:* Micrographs were taken on a Leica Stellaris 8 Falcon inverted microscope, provided by the Biological Imaging Institute within the Beckman Institute. Excitation was performed at 490 nm with the WLL laser operating at 20% gain and excitation was recorded at 516 nm. Resulting Z-stack images were analyzed in *ImageJ*.

#### ***4.5 Summary & Outlook***

In this chapter, we examined the micro-architected photoresist samples produced in Chapter 3 to assess their suitability for application in water filtration and to address the design goals outlined in Section 3.2. To address hydrophilicity, we examined the contact angle a water droplet forms with processed photoresist surfaces of both PGRO and SU-8, showing that PGRO produced a significantly shallower angle and indicating greater hydrophilicity than SU-8 produced structures. While we observed variation in the contact angle, we attributed that variation to inconsistent surface roughness that results from the many photoresist processing steps. We then explored membrane fluid transmission by examining videos of dyed droplets passing through the membrane, establishing that capillary action and the slight pressure afforded by

the droplet's surface tension yielded an approximate fluid flux of  $2.61 \pm 0.36 \text{ uL mm}^{-2} \text{ s}^{-1}$ . This proved undeniably that the produced films met design goal #2 and were capable of fluid transmission. To assess the functionalizability of the membrane and utility of the ONBAMA incorporation, samples were labelled with FITC dye and examined under confocal microscopy, confirming that the UV treatment successfully yielded deprotected amines that were reactive and capable of both analyte capture and further reaction. We additionally confirmed that this behavior was limited exclusively to regions excited by UV-C irradiation, confirming our hypothesis that ONBAMA could be utilized to lithographically functionalize polymer surfaces. This indicates that design goal #3 was sufficiently met as well. We therefore deem this a properly verified proof-of-concept.

Despite the success of these experiments, full characterization of the phenomena examined was not executed. Further experimentation is required, both to understand more precisely the flow behavior, where the flux of a droplet is maximized, for example. Additionally, bulk fluid flow through a membrane was not examined, where the entire surface of a membrane was subjected to a head pressure. Additionally, while the PGRO films did successfully exhibit localizable surface functionalization, little beyond phenomenological confirmation was achieved. Due to the auto-fluorescence of the polymer, functionalization and capture density could not be assessed. Attempts to measure FITC concentration in buffers after soaking yielded inconsistent and inconclusive results, since a great excess of FITC is required in solution to yield appreciable functionalization, no concentration change in solution was detected when examined under a fluorescent plate reader. To summarize, phenomenological confirmation of the hypotheses was achieved, but further work is required to better understand the quantitative efficacy of the described techniques. The overwhelming reason behind this lack of quantitative examination is the fragility of the membranes. At 5-10  $\mu\text{m}$  thick, membranes often cracked and flaked, or were not successfully delaminated from the substrate. In particular, the filtration experiments proved incredibly difficult to quantify, as ensuring a water-tight seal for

anything beyond a single droplet usually caused complete membrane failure. For these membranes to be utilized for commercial filtration applications, or even for more quantitative assessment of their filtration efficacy, produced membrane filters must be made more robust and capable of withstanding head pressures from imbibing fluids. Further discussion of how this might be achieved can be found in Chapter 5.

*Chapter 5*

## SUMMARY &amp; OUTLOOK

**5.1 Summary**

In this thesis, we explored the bulk lithographic fabrication of micro- and nano-architected polymer films with the goal to produce membrane water filters capable of facile and localizable surface functionalization for specific analyte targeting. We started by developing a holographic lithography technique for rapid manufacture of 3D nano-architected polymer sheets utilizing phase-shifting metasurface masks designed by our collaborators in the Faraon lab. By linearly raster scanning the masks with an unmodified 532 nm Gaussian beam, we demonstrated that submicron brick-and-mortar lattice-like periodic features could be resolved in negative-tone photoresist SU-8 at short timescales that more traditional fabrication techniques like two-photon lithography cannot achieve.<sup>[90-92]</sup> Recognizing the shortcomings of relying on SU-8 as a constituent material due to undesirable physical and chemical properties, we then designed and synthesized a novel substitute photoresist material consisting of a cross-linking enabler, glycidyl methacrylate, and a methacrylated *o*-nitrobenzyl-based photo-caged amine (ONBAMA) for facile post-processing surface functionalization. Each of the photoresist processing steps were then optimized according to relevant figures of merit. Soft bake time and duration was identified to be 10 min held at 75 °C by examining solvent content in spun films as the bake step proceeded. We identified the optical exposure dose of 0.55 W by evaluating the negative-tone resist's contrast of 2.85 with the Hurter-Driffield model, which indicated expected contrast compared to photoresists relying on comparable chemistry. We finally determined post-exposure bake conditions by evaluating the constituent polymer's glass transition temperature to be ~62 °C via differential scanning calorimetry.

With these established processing conditions, we demonstrated resolution of nominally 25  $\mu\text{m}$  circular pores for application as a water filtration membrane. While ideal feature resolution was not achieved, we deemed processing parameters sufficient for preliminary exploration of functionalization and filtration capabilities. We first confirmed that, despite their 5-10  $\mu\text{m}$  thickness, sufficiently wetted films could pass aqueous solutions via capillary forces, as predicted by COMSOL simulations and the Lucas-Washburn equation, demonstrating fluid flux of up to  $2.61 \pm 0.42 \text{ uL mm}^{-2} \text{ s}^{-1}$ . We then confirmed with bulk UV-exposure experiments and selective deprotection experiments the reactivity of liberated amines through labelling with a fluorescein isothiocyanate dye, indicating that ONBAMA-containing membranes do enable the largely unexplored phenomenon of post-processing localizable surface functionalization. Consequently, we demonstrated that GMA-based photoresists processed accordingly are potentially applicable as an affinity-based water filtration platform, and the remainder of this chapter will focus on future advancements of the technology toward that goal.

## ***5.2 Future Updates to Photoresist Processing & Formulation***

While the photoresist did successfully produce structures capable of isolating analytes from water and passing fluid, many improvements can be made to produce structures at greater resolution and smaller feature size. The first of these improvements might be to reconsider the soft bake temperature: we relied on the assumption that to successfully achieve small feature sizes, considerable solvent removal was necessary to minimize diffusion during subsequent bakes (and exposure) as much as possible; however, this may not have been the optimal approach. Studies exploring how soft-bake temperature affects polymerization temperature suggests that lower temperature soft bakes in turn lower necessary post-exposure bake temperature and have a secondary side effect of producing a more sensitive resist.<sup>[73]</sup> Exploration into soft-bake temperature is limited as it is believed that the post-exposure bake has a more pronounced effect on final material properties;

however, literature indicates that increasing solvent content of films has the added benefit of increasing resilience to shrinkage and internal stress development during later processing steps.<sup>[93-94]</sup> With respect to exposure, there are two points we would like to have explored further: the optimal dose, and the temperature of the mask. Regarding the former, we would have liked to explore a greater range of potential doses, noting that the apparent maximum dose from Figure 3.11 is not necessarily the optimal dose as was originally assumed. While it can be, optimal dose is more properly associated with feature resolution, such that a dose below the measured and observed  $D_0$  might provide maximum film thickness but swollen features, as it appears to in our case; perhaps a slightly lower dose might have provided a more ideal pore resolution.<sup>[75-76]</sup> Were a lower dose not to provide better resolution, examining the temperature of the mask, and more specifically the photoresist underlying the mask, would be of interest as well. As mentioned, in the more extreme exposure circumstances explored by this work, thermal cross-linking occurred due to the Cr mask elements absorbing considerable energy from the laser, and while that had evidently been reduced in later experiments, its elimination as a factor was never confirmed or pursued. Examining film temperature via thermocouples placed in resist films during exposures would provide useful insights into this source of uncertainty and would allow for evaluation of the optical dose's thermal load more quantitatively. While we believe that the post-exposure bake was reasonably well determined, with other processing modifications, we would re-evaluate the efficacy of the post-exposure bake in the context of more ideal conditions.

While processing parameters can address microscopic feature resolution, reformulation can address bulk material property concerns: or, more specifically, the difficulty that thin films provide. As was concluded in Chapter 4, despite the demonstrated efficacy of the films for analyte capture and water passage, the fragility of the produced filtering membranes proved to be difficult to manage. Films regularly cracked or cleaved during delamination, and additionally we observed material blowout during pressure loading experiments. Once the film was delaminated, it was

very difficult to maneuver and required care well beyond what a water filtering device should require. Consequently, a second-generation photoresist would ideally produce stronger and thicker films more amenable to bearing tensile loads. To accomplish this, we would aim to produce thicker films while simultaneously inducing a greater degree of cross-linking in films to produce stronger (albeit more brittle) membrane filters.<sup>[95-97]</sup> Regarding the former, to produce thicker films requires either conceding multiple spins, or increasing resist viscosity significantly. To increase viscosity, the primary means for doing so would be to increase the solids concentration of concentrated photoresist. 45% solids was initially selected because higher concentrations would inconsistently dissolve, often leaving either polymer or initiator undissolved at the bottom of the mixing vessel, and additionally for sufficiently thick films, an outer skin would develop on photoresists due to rapid drying at the surface. To compensate for this, finding an alternative solvent is likely the best option for producing more viscous photoresist; one that specifically meets the necessary criteria is  $\gamma$ -butyrolactone (GBL). While SU-8 advanced from GBL to cyclopentanone in its formulation history, we believe that the previously used solvent has advantages for large-molecule based photoresists: namely, considerably lower vapor pressure at room temperature.<sup>[98]</sup> A higher vapor pressure would reduce the evaporation rate and would allow for more uniform solvent removal, as well as finer control over solvent content within processed films. To facilitate polymer solubility and increase mass loading, reducing the molecular weight of the polymers further below 30 kDa is necessary, but to accomplish this would require further optimization of the ATRP process where Cu catalyst could be removed more consistently. To produce stronger, more resilient films requires hard baking at temperatures capable of inducing thermal cross-linking, a supplementary processing step often employed to increase lithographically manufactured structure strength. While cross-linking is known to be relatively low from just exposure and cationic polymerization alone, aiding cross-linking with thermal polymerization would produce more robust structures.<sup>[47]</sup>

### ***5.3 Future Application: Protein Capture***

This developed class of manufactured porous membranes can be further functionalized for incorporation into a variety of potential devices. For example, modification of the surface via biotinylation can allow for non-covalent capture of avidin-functionalized particles and other proteins for use in assays, protein purification, point-of-care diagnostic tools, and in drug delivery applications.<sup>[99]</sup> Biotin agents are typically produced with an N-hydroxysuccinimide (NHS) or N-hydroxysulfosuccinimide (sulfo-NHS) moiety to facilitate reaction with amines for facile protein attachment via NHS coupling, but we could utilize this affinity for primary (and secondary) amines to functionalize the surface of poly(GMA-*rand*-ONBAMA) structures with biotin, according to the simple reaction scheme shown below in Figure 5.1.<sup>[100-101]</sup> Membranes functionalized in this manner can then participate in the wide array of available applications, including ELISA assays, protein isolation, and antibody detection. Additionally, a membrane or surface functionalized in this manner could reasonably serve as a stationary phase in automated assays and elution-based protein analysis techniques.<sup>[102-104]</sup> Serving as either a coating or as membrane filter, materials manufactured with this chemistry allow for the development of complex fluidic platforms with selectively and locally patterned surface chemistries. Given the nature of their fabrication method, we envision large-scale manufacture of biotinylated nano-architectures, incorporating chemical hierarchy with localizable deprotection, to allow access to underserved commercial applications utilizing the material and techniques pioneered in this thesis.

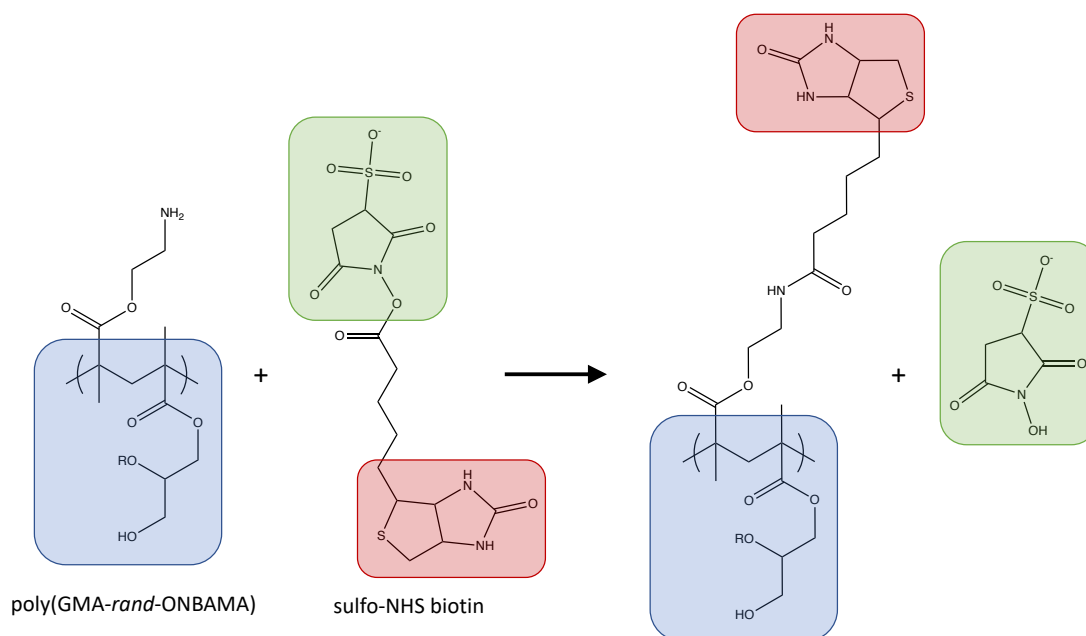


**Figure 5.1:** Surface biotinylation of PGRO. A membrane produced via techniques outlined in Chapter 3 followed by the necessary hard bake to open remaining epoxides results in a fully cross-linked polymer photoresist with no remaining epoxides (blue box). Exposure with UV-C deprotects the ONBAMA amine and enables reaction with sulfo-NHS (green box) functionalized biotin (red box). The sulfo-NHS acts as a leaving group while the amine covalently bonds to the biotin via its spacer arm, resulting in fully biotinylated membrane.

## BIBLIOGRAPHY

- [1] Saini, Priyanka, Vijaya Kumar Bulasara, and Akepati S. Reddy. "Performance of a new ceramic microfiltration membrane based on kaolin in textile industry wastewater treatment." *Chemical Engineering Communications* 206.2 (2019): 227-236.
- [2] Rouquie, Camille, et al. "Immersed membranes configuration for the microfiltration of fruit-based suspensions." *Separation and Purification Technology* 216 (2019): 25-33.
- [3] Brown, A. I., et al. "Membrane pleating effects in 0.2  $\mu\text{m}$  rated microfiltration cartridges." *Journal of Membrane Science* 341.1-2 (2009): 76-83.
- [4] Wang, Yifei, et al. "Carbon nanotube composite membranes for microfiltration of pharmaceuticals and personal care products: Capabilities and potential mechanisms." *Journal of Membrane Science* 479 (2015): 165-174.
- [5] Anis, Shaheen Fatima, Raed Hashaikeh, and Nidal Hilal. "Microfiltration membrane processes: A review of research trends over the past decade." *Journal of Water Process Engineering* 32 (2019): 100941.
- [6] Ahmed, Rameez, et al. "Graphene-based bacterial filtration via electrostatic adsorption." *Advanced Materials Interfaces* 9.6 (2022): 2101917.
- [7] Celebioglu, Asli, Zehra Irem Yildiz, and Tamer Uyar. "Electrospun crosslinked poly-cyclodextrin nanofibers: Highly efficient molecular filtration thru host-guest inclusion complexation." *Scientific Reports* 7.1 (2017): 7369.
- [8] Fu, Weigui, et al. "Highly hydrophilic poly (vinylidene fluoride) ultrafiltration membranes modified by poly (N-acryloyl glycinamide) hydrogel based on multi-hydrogen bond self-assembly for reducing protein fouling." *Journal of Membrane Science* 572 (2019): 453-463.
- [9] Li, Chen, et al. "Ceramic nanocomposite membranes and membrane fouling: A review." *Water Research* 175 (2020): 115674.
- [10] Zhu, Fan, et al. "A critical review on the electrospun nanofibrous membranes for the adsorption of heavy metals in water treatment." *Journal of Hazardous Materials* 401 (2021): 123608.

- [11] Kerr-Phillips, Thomas, Benjamin Schon, and David Barker. "Polymeric materials and microfabrication techniques for liquid filtration membranes." *Polymers* 14.19 (2022): 4059.
- [12] Shin, Suyong, et al. "Dimensionally controlled water-dispersible amplifying fluorescent polymer nanoparticles for selective detection of charge-neutral analytes." *Polymer Chemistry* 8.48 (2017): 7507-7514.
- [13] del Barrio, Jesús, and Carlos Sánchez-Somolinos. "Light to shape the future: From photolithography to 4D printing." *Advanced Optical Materials* 7.16 (2019): 1900598.
- [14] Holdich, Richard, et al. "Pore design and engineering for filters and membranes." *Philosophical Transactions of the Royal Society A: Mathematical, Physical and Engineering Sciences* 364.1838 (2006): 161-174.
- [15] Meza, Lucas R., Satyajit Das, and Julia R. Greer. "Strong, lightweight, and recoverable three-dimensional ceramic nanolattices." *Science* 345.6202 (2014): 1322-1326.
- [16] Miyake, Masao, et al. "Fabrication of three-dimensional photonic crystals using multibeam interference lithography and electrodeposition." *Advanced Materials* 21.29 (2009): 3012-3015.
- [17] Park, Sung-Gyu, et al. "Cu<sub>2</sub>O inverse woodpile photonic crystals by prism holographic lithography and electrodeposition." *Advanced Materials* 23.24 (2011): 2749-2752.
- [18] Chang, Chih-Hao, et al. "From two-dimensional colloidal self-assembly to three-dimensional nanolithography." *Nano Letters* 11.6 (2011): 2533-2537.
- [19] Bagal, Abhijeet, et al. "Large-area nanolattice film with enhanced modulus, hardness, and energy dissipation." *Scientific Reports* 7.1 (2017): 9145.
- [20] Bae, Gwangmin, Dongchan Jang, and Seokwoo Jeon. "Scalable fabrication of high-performance thin-shell oxide nanoarchitected materials via proximity-field nanopatterning." *ACS Nano* 15.3 (2021): 3960-3970.

- [21] Kamali, Seyedeh Mahsa, et al. "Metasurface-generated complex 3-dimensional optical fields for interference lithography." *Proceedings of the National Academy of Sciences* 116.43 (2019): 21379-21384.
- [22] Crivello, James V., and J. H. W. Lam. "Diaryliodonium salts. A new class of photoinitiators for cationic polymerization." *Macromolecules* 10.6 (1977): 1307-1315.
- [23] Crivello, James V. "The discovery and development of onium salt cationic photoinitiators." *Journal of Polymer Science Part A: Polymer Chemistry* 37.23 (1999): 4241-4254.
- [24] Zheldakov, Igor L., et al. "Transient Spectroscopy of 5, 7-diiodo-3-butoxy-6-fluorone (DIBF)." *Photochemistry and Photobiology* 90.2 (2014): 335-337.
- [25] Mack, Chris A. "Optical lithography." *Bellingham: SPIE Field Guides* (2006).
- [26] Meisel, Daniel Christoph, et al. "Shrinkage precompensation of holographic three-dimensional photonic-crystal templates." *Advanced Materials* 18.22 (2006): 2964-2968.
- [27] Pang, Yee Kwong, et al. "Chiral microstructures (spirals) fabrication by holographic lithography." *Optics Express* 13.19 (2005): 7615-7620.
- [28] Denning, Robert G., et al. "The control of shrinkage and thermal instability in SU-8 photoresists for holographic lithography." *Advanced Functional Materials* 21.9 (2011): 1593-1601.
- [29] Barber, Richard L., et al. "Optimisation of SU-8 processing parameters for deep X-ray lithography." *Microsystem Technologies* 11 (2005): 303-310.
- [30] Yokoyama, Takahiro, et al. "Plasmon-enhanced photopolymerization of SU-8 on rough gold surfaces." *The Journal of Physical Chemistry C* 114.46 (2010): 19596-19599.
- [31] Lee, Cheng-Tsung, Richard A. Lawson, and Clifford L. Henderson. "Understanding the effects of photoacid distribution homogeneity and diffusivity on critical dimension control and line edge roughness in chemically amplified resists." *Journal of Vacuum Science & Technology B: Microelectronics and Nanometer Structures Processing, Measurement, and Phenomena* 26.6 (2008): 2276-2280.

- [32] Itani, Toshiro, et al. "Relationship between remaining solvent and acid diffusion in chemically amplified deep ultraviolet resists." *Japanese Journal of Applied Physics* 35.12S (1996): 6501.
- [33] Mack, Chris A., et al. "Modeling solvent diffusion in photoresist." *Journal of Vacuum Science & Technology B: Microelectronics and Nanometer Structures Processing, Measurement, and Phenomena* 16.6 (1998): 3779-3783.
- [34] Tao, Sarah L., et al. "Surface modification of SU-8 for enhanced biofunctionality and nonfouling properties." *Langmuir* 24.6 (2008): 2631-2636.
- [35] Sameoto, Dan, et al. "Control of the out-of-plane curvature in SU-8 compliant microstructures by exposure dose and baking times." *Journal of Micromechanics and Microengineering* 17.5 (2007): 1093.
- [36] Barra, Monica, et al. "On the photodecomposition mechanism of o-diazonaphthoquinones." *Journal of the American Chemical Society* 114.7 (1992): 2630-2634.
- [37] Roy, Debmalya, et al. "DNQ–novolac photoresists revisited: 1H and 13C NMR evidence for a novel photoreaction mechanism." *Magnetic Resonance in Chemistry* 41.2 (2003): 84-90.
- [38] Lee, E. H., et al. "LET effect on cross-linking and scission mechanisms of PMMA during irradiation." *Radiation Physics and Chemistry* 55.3 (1999): 293-305.
- [39] Shultz, Allan R. "Degradation of polymethyl methacrylate by ultraviolet light." *The Journal of Physical Chemistry* 65.6 (1961): 967-972.
- [40] Pirman, Tomaz, et al. "Radical polymerization of acrylates, methacrylates, and styrene: Biobased approaches, mechanism, kinetics, secondary reactions, and modeling." *Industrial & Engineering Chemistry Research* 60.26 (2021): 9347-9367.
- [41] Carbaugh, Daniel J., Savas Kaya, and Faiz Rahman. "Transparent and visible light-insensitive acrylic photoresist for negative tone optical lithography." *Journal of Vacuum Science & Technology B, Nanotechnology and Microelectronics: Materials, Processing, Measurement, and Phenomena* 35.1 (2017): 011601.

- [42] Clark, Tolecia, et al. "Photopolymerization of thiol-ene systems based on oligomeric thiols." *Journal of Polymer Science Part A: Polymer Chemistry* 47.1 (2009): 14-24.
- [43] Cole, Megan A., and Christopher N. Bowman. "Synthesis and characterization of thiol-ene functionalized siloxanes and evaluation of their crosslinked network properties." *Journal of Polymer Science Part A: Polymer Chemistry* 50.20 (2012): 4325-4333.
- [44] Sienel, Guenter, Robert Rieth, and Kenneth T. Rowbottom. "Epoxides." *Ullmann's Encyclopedia of Industrial Chemistry* (2000).
- [45] Penczek, Stanisław, Przemysław Kubisa, and Krzysztof Matyjaszewski, eds. *Cationic Ring-Opening Polymerization: 2. Synthetic Applications*. Berlin, Heidelberg: Springer Berlin Heidelberg, 1985.
- [46] Shaw, Jane M., et al. "Negative photoresists for optical lithography." *IBM Journal of Research and Development* 41.1.2 (1997): 81-94.
- [47] Hayek, Ali, et al. "Poly (glycidyl methacrylate) s with controlled molecular weights as low-shrinkage resins for 3D multibeam interference lithography." *Journal of Materials Chemistry* 18.28 (2008): 3316-3318.
- [48] Kim, Kwanghyun, et al. "Highly transparent poly (glycidyl methacrylate-co-acryloisobutyl POSS) for 100  $\mu\text{m}$ -thick submicron patterns with an aspect ratio over 100." *Chemical Communications* 53.58 (2017): 8172-8175.
- [49] Moon, Jun Hyuk, et al. "Colloidal lithography with crosslinkable particles: fabrication of hierarchical nanopore arrays." *Chemical Communications* 32 (2005): 4107-4109.
- [50] Lou, Qin, and Devon A. Shipp. "Poly (glycidyl methacrylate-block-styrene) for photolithographically patternable resist materials." *Progress in Controlled Radical Polymerization: Materials and Applications*. American Chemical Society, 2012. 115-125.
- [51] Klimov, Viktor V., et al. "Effect of the composition of copolymers Based on glycidyl methacrylate and fluoroalkyl methacrylates on the free energy and lyophilic properties of the modified surface." *Polymers* 14.10 (2022): 1960.

- [52] Scriven, L. E. Physics and applications of dip coating and spin coating. *MRS Online Proceedings Library* **121**, 717–729 (1988).
- [53] Danglad-Flores, José, Stephan Eickelmann, and Hans Riegler. "Deposition of polymer films by spin casting: A quantitative analysis." *Chemical Engineering Science* 179 (2018): 257-264.
- [54] Arscott, Steve. "The limits of edge bead planarization and surface levelling in spin-coated liquid films." *Journal of Micromechanics and Microengineering* 30.2 (2020): 025003.
- [55] Yasui, Manabu, et al. "Effects of post exposure bake temperature and exposure time on SU-8 nanopattern obtained by electron beam lithography." *Japanese Journal of Applied Physics* 53.11S (2014): 11RF03.
- [56] Feng, Ru, and Richard J. Farris. "Influence of processing conditions on the thermal and mechanical properties of SU8 negative photoresist coatings." *Journal of Micromechanics and Microengineering* 13.1 (2002): 80.
- [57] Wouters, Kristof, and Robert Puers. "Diffusing and swelling in SU-8: insight in material properties and processing." *Journal of Micromechanics and Microengineering* 20.9 (2010): 095013.
- [58] Blagoi, Gabriela, et al. "Functionalization of SU-8 photoresist surfaces with IgG proteins." *Applied Surface Science* 255.5 (2008): 2896-2902.
- [59] Aekbote, Badri Lakshmanrao, et al. "Aminosilane-based functionalization of two-photon polymerized 3D SU-8 microstructures." *European Polymer Journal* 48.10 (2012): 1745-1754.
- [60] Anbumani, Silambarasan, et al. "Oxygen plasma-enhanced covalent biomolecule immobilization on SU-8 thin films: A stable and homogenous surface biofunctionalization strategy." *Applied Surface Science* 553 (2021): 149502.
- [61] Nagaiyanallur, Venkataraman V., et al. "Tailoring SU-8 surfaces: Covalent attachment of polymers by means of nitrene insertion." *Langmuir* 30.33 (2014): 10107-10111.
- [62] Kellum, Matthew G., et al. "Stimuli-responsive micelles of amphiphilic AMPS-b-AAL copolymers in layer-by-layer films." *Journal of Polymer Science Part A: Polymer Chemistry* 49.5 (2011): 1104-1111.

- [63] Hoenders, Daniel, Thomas Tigges, and Andreas Walther. "Combining the incompatible: Block copolymers consecutively displaying activated esters and amines and their use as protein-repellent surface modifiers with multivalent biorecognition." *Polymer Chemistry* 6.3 (2015): 476-486.
- [64] Mazrad, Zihnil A. I., et al. "Protected amine-functional initiators for the synthesis of  $\alpha$ -amine homo- and heterotelechelic poly (2-ethyl-2-oxazoline)s." *Polymer Chemistry* 13.30 (2022): 4436-4445.
- [65] Freeman, C. E., and A. G. Howard. "Measurement of the Fmoc loading of protected amine-functionalised polymer beads." *Talanta* 65.2 (2005): 574-577.
- [66] Watuthantrige, Nethmi De Alwis, Pierce N. Kurek, and Dominik Konkolewicz. "Photolabile protecting groups: a strategy for making primary amine polymers by RAFT." *Polymer Chemistry* 9.13 (2018): 1557-1561.
- [67] Tsarevsky, Nicolay V., & Wojciech Jakubowski. (2011). *Journal of Polymer Science Part A: Polymer Chemistry*, 49(4), 918-925.
- [68] Lee, Jung A., et al. "Fabrication and characterization of freestanding 3D carbon microstructures using multi-exposures and resist pyrolysis." *Journal of Micromechanics and Microengineering* 18.3 (2008): 035012.
- [69] Despont, Michel, et al. "High-aspect-ratio, ultrathick, negative-tone near-UV photoresist for MEMS applications." *Proceedings IEEE The Tenth Annual International Workshop on Micro Electro Mechanical Systems. An Investigation of Micro Structures, Sensors, Actuators, Machines and Robots*. IEEE, 1997.
- [70] Liu, Gang, et al. "Fabrication of high-aspect-ratio microstructures using SU8 photoresist." *Microsystem Technologies* 11 (2005): 343-346.
- [71] Anhoj, Thomas A., et al. "The effect of soft bake temperature on the polymerization of SU-8 photoresist." *Journal of Micromechanics and Microengineering* 16.9 (2006): 1819.
- [72] Lee, Jeong Bong, Kyung-Hak Choi, and Koangki Yoo. "Innovative SU-8 lithography techniques and their applications." *Micromachines* 6.1 (2014): 1-18.

- [73] Hurter, Ferdinand & Vero Charles Driffield, "Photochemical investigations and a new method of determination of the sensitiveness of photographic plates," *Journal of the Society of Chemical Industry*, (1890): 455-469.
- [74] Ma, Yaqi, et al. "Processing study of SU-8 pillar profiles with high aspect ratio by electron-beam lithography." *Microelectronic Engineering* 149 (2016): 141-144.
- [75] Lawson, Richard A., et al. "Optimizing performance in cross-linking negative-tone molecular resists." *Advances in Patterning Materials and Processes XXXII*. Vol. 9425. SPIE, 2015.
- [76] Narcross, Hannah, et al. "Effect of molecular resist structure on glass transition temperature and lithographic performance in epoxide functionalized negative tone resists." *Advances in Patterning Materials and Processes XXXII*. Vol. 9425. SPIE, 2015.
- [77] Saiter, Jean Marc, et al. "Glass transition temperature and value of the relaxation time at T<sub>g</sub> in vitreous polymers." *Macromolecular Symposia*. Vol. 258. No. 1. Weinheim: WILEY-VCH Verlag, 2007.
- [78] Hutchinson, John. "Determination of the glass transition temperature: Methods correlation and structural heterogeneity." *Journal of Thermal Analysis and Calorimetry* 98.3 (2009): 579-589.
- [79] Ainslie, Kristy M., et al. "Microfabricated devices for enhanced bioadhesive drug delivery: Attachment to and small-molecule release through a cell monolayer under flow." *Small* 5.24 (2009): 2857-2863.
- [80] Zhang, Hongji, Hesheng Xia, and Yue Zhao. "Optically triggered and spatially controllable shape-memory polymer-gold nanoparticle composite materials." *Journal of Materials Chemistry* 22.3 (2012): 845-849.
- [81] Cai, Jianchao, et al. "Lucas-Washburn equation-based modeling of capillary-driven flow in porous systems." *Langmuir* 37.5 (2021): 1623-1636.
- [82] de Gennes, Pierre-Gilles, et al. "Capillarity and gravity." *Capillarity and Wetting Phenomena: Drops, Bubbles, Pearls, Waves* (2004): 33-67.

- [83] Hamraoui, Ahmed, and Tommy Nylander. "Analytical approach for the Lucas–Washburn equation." *Journal of Colloid and Interface Science* 250.2 (2002): 415-421.
- [84] Fries, N., and M. Dreyer. "An analytic solution of capillary rise restrained by gravity." *Journal of Colloid and Interface Science* 320.1 (2008): 259-263.
- [85] Nakae, Hideo, et al. "Effects of surface roughness on wettability." *Acta Materialia* 46.7 (1998): 2313-2318.
- [86] Chen, Xue, et al. "Water droplet spreading and wicking on nanostructured surfaces." *Langmuir* 33.27 (2017): 6701-6707.
- [87] Hertaeg, Michael J., et al. "Dynamics of stain growth from sessile droplets on paper." *Journal of Colloid and Interface Science* 541 (2019): 312-321.
- [88] Chaganti, Lalith K., Navneet Venkatakrishnan, and Kakoli Bose. "An efficient method for FITC labelling of proteins using tandem affinity purification." *Bioscience Reports* 38.6 (2018).
- [89] Hungerford, Graham, et al. "Effect of the labelling ratio on the photophysics of fluorescein isothiocyanate (FITC) conjugated to bovine serum albumin." *Photochemical & Photobiological Sciences* 6.2 (2007): 152-158.
- [90] Bunea, Ada-Ioana, et al. "Micro 3D printing by two-photon polymerization: Configurations and parameters for the nanoscribe system." *Micro*. Vol. 1. No. 2. MDPI, 2021.
- [91] Kotz, Frederik, et al. "Two-photon polymerization of nanocomposites for the fabrication of transparent fused silica glass microstructures." *Advanced Materials* 33.9 (2021): 2006341.
- [92] Faraji Rad, Zahra, Philip D. Prewett, and Graham J. Davies. "High-resolution two-photon polymerization: The most versatile technique for the fabrication of microneedle arrays." *Microsystems & Nanoengineering* 7.1 (2021): 71.
- [93] Keller, Stephan, et al. "Processing of thin SU-8 films." *Journal of Micromechanics and Microengineering* 18.12 (2008): 125020.

- [94] Johari, Shazlina, et al. "The effect of softbaking temperature on SU-8 photoresist performance." *2014 IEEE International Conference on Semiconductor Electronics (ICSE2014)*. IEEE, 2014.
- [95] Jayaram, Robin C., Aakansha Vishnoi, and Krishna N. Jonnalagadda. "Mechanical behavior and anisotropy of spin-coated SU-8 thin films for MEMS." *Journal of Microelectromechanical Systems* 23.1 (2013): 168-180.
- [96] Liu, Chenpu, et al. "Understanding fracture behavior of epoxy-based polymer using molecular dynamics simulation." *Journal of Molecular Graphics and Modelling* 101 (2020): 107757.
- [97] Winterstein, Thomas, et al. "SU-8 electrothermal actuators: Optimization of fabrication and excitation for long-term use." *Micromachines* 5.4 (2014): 1310-1322.
- [98] Shaw, Mark, et al. "Improving the process capability of SU-8." *Microsystem Technologies* 10.1 (2003): 1-6.
- [99] Gao, Feng, et al. "Leveraging avidin-biotin interaction to quantify permeability property of microvessels-on-a-chip networks." *American Journal of Physiology-Heart and Circulatory Physiology* 322.1 (2022): H71-H86.
- [100] Fischer, Marcel J. E. "Amine coupling through EDC/NHS: A practical approach." *Surface Plasmon Resonance: Methods and Protocols* (2010): 55-73.
- [101] Orelma, Hannes, et al. "Generic method for attaching biomolecules via avidin-biotin complexes immobilized on films of regenerated and nanofibrillar cellulose." *Biomacromolecules* 13.9 (2012): 2802-2810.
- [102] Collé, Allain, et al. "Cystatin C levels in sera of patients with human immunodeficiency virus infection. A new avidin-biotin ELISA assay for its measurement." *Journal of Immunoassay and Immunochemistry* 13.1 (1992): 47-60.
- [103] Sutton, Ann, et al. "An avidin-biotin based ELISA for quantitation of antibody to bacterial polysaccharides." *Journal of Immunological Methods* 82.2 (1985): 215-224.

- [104] Shekarchi, I. C., et al. "Avidin-biotin latex agglutination assay for detection of antibodies to viral antigens." *Journal of Clinical Microbiology* 26.5 (1988): 954-95.